Open access • Journal Article • DOI:10.1017/JFM.2013.83

Turbulent wake past a three-dimensional blunt body. Part 1. Global modes and bi-stability — Source link

Mathieu Grandemange, Marc Gohlke, Olivier Cadot

Published on: 01 May 2013 - Journal of Fluid Mechanics (Cambridge University Press)

Topics: Strouhal number, Vortex shedding, Wake, Drag and Reynolds number

Turbulent wake past a three-dimensional blunt body. Part 1. Global modes and bi-stability

Mathieu Grandemange, Marc Gohlke, Olivier Cadot

Turbulent wake past a three-dimensional blunt body. Part 1. Global modes and bi-stability.

M. GRANDEMANGE[1,2]†, M. GOHLKE[2] AND O. CADOT[1]

[1]Unité de Mécanique, Ecole Nationale Supérieure de Techniques Avancées, ParisTech, Chemin de la Hunière, 91761 Palaiseau Cedex, France

[2]PSA Peugeot Citroën, Centre Technique de Velizy, Route de Gisy, 78943 Vélizy-Villacoublay Cedex, France

(Received ?; revised ?; accepted ?. - To be entered by editorial office)

The flow around the three-dimensional blunt geometry presented in the work of Ahmed *et al.* (1984) is investigated experimentally at Re $= U_0H/\nu = 9.2\ 10^4$. The massive recirculation on the base responsible for a dominant part of the drag is characterized. The analyses of the coherent dynamics of the wake reveal the presence of two very distinctive timescales. At long timescales $T_l \sim 10^3 H/U_0$, the recirculation region shifts between two preferred reflectional symmetry breaking positions leading to a statistical symmetric wake; the succession of these asymmetric states is random. This bi-stable behavior is independent of the Reynolds number but occurs only over a critical value of ground clearance. At short timescales $T_s \sim 5H/U_0$, the wake presents weak coherent oscillations in the vertical and lateral directions. They are respectively associated with the interaction of the top / bottom and lateral shear layers; when normalized by the height and width of the body, the Strouhal numbers are close to 0.17. These results suggest an alternate shedding associated with the vertical oscillation and a one-sided vortex shedding in the lateral direction with an orientation linked to the current asymmetric position. Finally, the impact of these coherent wake motions on the base pressure is discussed to orient further drag reduction strategies.

1. Introduction

Many industrial flows are produced by the motion of bluff bodies in a fluid. The simplest cases that are frequently used can be found in the transport industries, especially for ground vehicles such as trains, cars or lorries. The bluffness associated with a functional blunt shape provokes a massive flow separation and consequently complex wake dynamics. Over the past three decades, the growing constraints on energy have motivated research activities to improve the understanding of fundamental notions such as stability or force intensities in the wake of basic geometries. The objective is then to limit the unwanted effect of the flow through optimization of the geometry or control strategies. In the precise case of the automotive geometries, the work of Ahmed *et al.* (1984) paved the way to the comprehension of the flow around different shapes of road vehicles by showing the critical influence of the afterbody configuration. In the case of moderate slant angles of rear window (from 12.5° to 30°), a pair of intense counter-rotating vortices develop in the wake of the model reducing the pressure on the afterbody. In the worst configuration (slant angle close to 30°), these structures induce up to 50% increase

† Email address for correspondence: mathieu.grandemange@ensta-paristech.fr

in drag in comparison to the 0° case. As similar flow structures are reported in the wakes of notch-back and fast-back vehicles (Hucho 1998), important work is devoted to the drag reduction of the 25° slant angle body through various passive and active control strategies such as splitter plates (Gilliéron & Kourta 2010), flaps (Beaudoin & Aider 2008; Fourrié *et al.* 2011), boundary layer streaks (Pujals *et al.* 2010) or even pulsed jets (Bruneau *et al.* 2011).
On the other hand, for slant angles below 10°, the topology is characterized by a massive recirculation bubble on the base. This region, associated with low levels of base pressure, is the major contributor to the aerodynamic drag. The autopower spectra of the base pressure signals, mixing layer velocities or force measurements show characteristic frequencies of the natural wake. The following analyses are reported in literature but the nature of the corresponding large scale wake structures is still unclear.

- A low frequency dynamics at Strouhal number ($\mathrm{St} = fH/U_0$) close to 0.07 is measured experimentally (Duell & George 1999; Khalighi *et al.* 2001, 2012) and interpreted as a periodic interaction between the upper and lower part of the trapped toric vortex in the near wake; a shedding of pairs of vortices from the trailing edge with a lateral oscillation are also hypothesized (Khalighi *et al.* 2001).
- The numerical simulations of Bayraktar *et al.* (2001) evidence two frequencies are Strouhal numbers 0.106 and 0.086 in the unsteady measurements of the lift force and side force respectively but their organization is not discussed.
- The work of Khalighi *et al.* (2012) reports a coherent motion at St = 0.17 downstream of the recirculation region with a peak of energy particularly clear when the probe is in the plane of symmetry.
- A high frequency mode is observed by Duell & George (1999) at St = 1.157 and interpreted as a shedding of vortices from the mixing layers with a pseudo-helical structure.

Over such geometry, literature also reports the use of different efficient control devices. Using splitter plates, Khalighi *et al.* (2001) achieved 20% drag reduction associated with a decrease in the unsteadiness of the wake for both coherent and turbulent structures. In addition, the parametric study on chamfer angles performed by Littlewood & Passmore (2010) highlights the sensitivity of the flow to the trailing edge shape; this high sensitivity of the drag to the initial characteristics of the mixing layer is confirmed by the promising numerical work of active control performed by Rouméas *et al.* (2009), Bruneau *et al.* (2010) and Wassen *et al.* (2010) that enable to reach up to 30% drag reduction. However, the mechanisms responsible for the selection of the base pressure remain to be clarified. In particular, the physics of mixing layer development and the effect of the global modes in the wake are still open issues.

More generally, important fundamental work is dedicated to three-dimensional bluff geometries even if these wakes are poorly documented in comparison to the flourishing literature devoted to the Von-Kármán street past cylinders. The wake past axisymmetric geometries undergoes several transitions as the Reynolds number increases leading to an unsteady turbulent wake (Sakamoto & Haniu 1990). The high frequency mixing layer instabilities in the near wake degenerate into large scale vortex loops developing from the end of the recirculation bubble; the wake oscillates randomly (Taneda 1978; Sakamoto & Haniu 1990) and may have a helical structure highly coherent in space (Pao & Kao 1977; Berger *et al.* 1990; Yun *et al.* 2006). This unsteady global mode is reported at $0.1 < fD/U_0 < 0.2$ depending on geometry and Reynolds number.
Over more complex geometries, global modes may also be observed but their frequencies and structures are slightly different. Kiya & Abe (1999) depicted the impact of the as-

pect ratio on the vortex shedding in the wake of elliptical and rectangular normal flat plates. Two peaks of energy are observed in the power spectrum of velocity signals at Strouhal numbers between 0.05 and 0.15 depending on the aspect ratio. They correspond to oscillations of the wake in the two crossflow directions. Changing the hot-wire probe location, one or the other or even both unsteady modes are measured.
Besides, such global dynamics are affected by wall proximity: the recent work of Ruiz *et al.* (2009) studying the unsteady near wake of a disk normal to a wall show an increase in the complexity of the flow as the gap ratio decreases. The vertical wake oscillation is progressively attenuated and combined with a slight increase in the shedding frequency. Eventually, Ruiz *et al.* (2009) found a critical gap ratio under which the vertical oscillation of the disk wake is suppressed and a separation occurs on the ground associated with a low frequency dynamics at St ~ 0.03. Past a square-back three-dimensional geometry, a change in the wake topology is equally observed through the base pressure distribution when the gap ratio is particularly small in presence of a fixed ground (Duell & George 1993).

Recently Grandemange *et al.* (2012*b*) showed the critical impact of imperfections in the axisymmetry of the set-up on the wake. Due to the support, the wake selects two preferred positions and shifts randomly between them after a large amount of shedding. The statistical symmetry of the set-up is preserved but strongly depends on residual asymmetries. Such a high sensitivity to the symmetry was equally described in the flow past three-dimensional double backward facing step (Herry *et al.* 2011). In parallel, high degrees of asymmetry have been observed in the flow over road vehicle shapes: the experiments of Lawson *et al.* (2007) report asymmetric recirculation bubble on a rear window of a notch-back model and the numerical simulations of Wassen *et al.* (2010) presents unexpected lateral asymmetries in the recirculating flow. The latest developments of Grandemange *et al.* (2012*a*) evidenced that the origins of such symmetry breaking past a square back Ahmed geometry is associated with bifurcations in the laminar flow but the ingredients for such a multi-stability and the associated dynamics are still to be detailed.

The present work aims at clarifying the flow past the square back geometry presented in the experiments of Ahmed *et al.* (1984). It is currently massively used to develop flow control strategies; nevertheless the clear description of the coherent dynamics of the wake has not been reported in literature. Thus, the results are to be used as a reference for the characterization of the global modes and bi-stability of the flow; the present analyses should be considered to develop efficient flow control strategies needed by industry. In addition, these experiments introduce the basis for the sensitivity analyses of the wake that are to be detailed in a second communication.

The article is organized as follows. In section 2, the experimental setup and measurements are presented. Then, section 3 is devoted to the results: analysis of the mean properties of the flow (3.1) and investigation of the coherent wake dynamics (3.2). These results are discussed in section 4 and eventually, concluding remarks are presented in section 5.

2. Experimental set-up

2.1. *Geometry*

The geometry of the set-up is presented in figure 1. A ground plate is placed in an Eiffel type wind tunnel to form a 3/4 open jet facility. The turbulent intensity is less than 0.3% and the homogeneity of the velocity over the 390 mm $\times$ 400 mm test section is 0.4%. The wake is generated by a square-back geometry used in the experiments of Ahmed *et al.* (1984) at scale 1/4. The total length of the body is $L = 261.0$ mm, the height H and width W of the base are respectively 72.0 mm and 97.2 mm. The four supports are cylindrical with a diameter of 7.5 mm and the ground clearance is set at $C = 12.5$ mm to match the reference experiments. The blockage ratio is less than 5%. The coordinate system is defined as x in the streamwise direction, z normal to the ground and y forming a direct trihedral.
In order to have constant flow conditions, the ground plate is placed at 10 mm over the lower face of the inlet and triggers the turbulent boundary layer 140 mm upstream of the forebody without separation at the leading edge. When the body is not in the test section, the ground boundary layer thickness based on 99% of the free-flow velocity at $x = -L$, *i.e.* 140 mm downstream of the leading edge, is $\delta_{0.99} = 6.3$ mm with a precision of 0.1 mm; the displacement and momentum thicknesses are 0.89 ± 0.05 mm and 0.60 ± 0.02 mm respectively.

The main flow velocity is $U_0 = 20$ m s^{-1} and the Reynolds number based on H (Re $= U_0H/\nu$) is 9.2 10^4. The velocities are defined as $\vec{u} = u_x.\vec{e_x} + u_y.\vec{e_y} + u_z.\vec{e_z}$; $u_{ij} = \sqrt{{u_i}^2 + {u_j}^2}$ is the amplitude of velocity at the considered point in the plane $(\vec{e_i},\vec{e_j})$. A or $\langle a \rangle$ and $Std(a)$ are respectively average value and standard deviation of any quantity a; $a' = a - A$ is the fluctuating part of a. The height of the base H, density ρ and inlet velocity U_0 are used to obtain non-dimensional values marked with an asterisk.

Flying probes are mounted on three-dimensional displacement systems made up of three Newport (M-)MTM long travel consoles controlled by the Newport Motion Controller ESP301; the precision of the robots is better than 0.1 mm.

2.2. *Pressure measurements*

The pressure on the body is measured at 62 locations. The taps are distributed to get the pressure gradients on the nose and the repartition of base pressure. 21 taps are located on the base of the body; 41 others give the pressure distribution on the nose and on the sides in the plane $y^* = 0$ and in the plane $z^* = 0.67$ (which correspond to the mid-height of the geometry). The pressure is obtained using a 64 port HD miniature pressure scanner and a SCANdaq 8000 interface connected to a PC with Labview software. The pressure scanner takes 50 pressure samples per second and the measurement is automatically averaged over 1 s. The accuracy of the measurement at 1 Hz is then ± 3 Pa. The pressure scanner is located inside the model so that it is linked to each tap with less than 250 mm of vinyl tube to limit the filtering effect of the tubing; it is denoted "P scan" in figures 1(a)–(b). It is then connected to the measurement chain using a wire going through a front support of the model so that, apart from the supports, nothing disturbs the under-body flow.

Besides, the pressure in the wake is measured through the six static ports of a Prandtl tube mounted on a displacement robot and connected to a Scanivalve DSA 3217/16px device. The pressure is considered without any correction so the result is only ac-

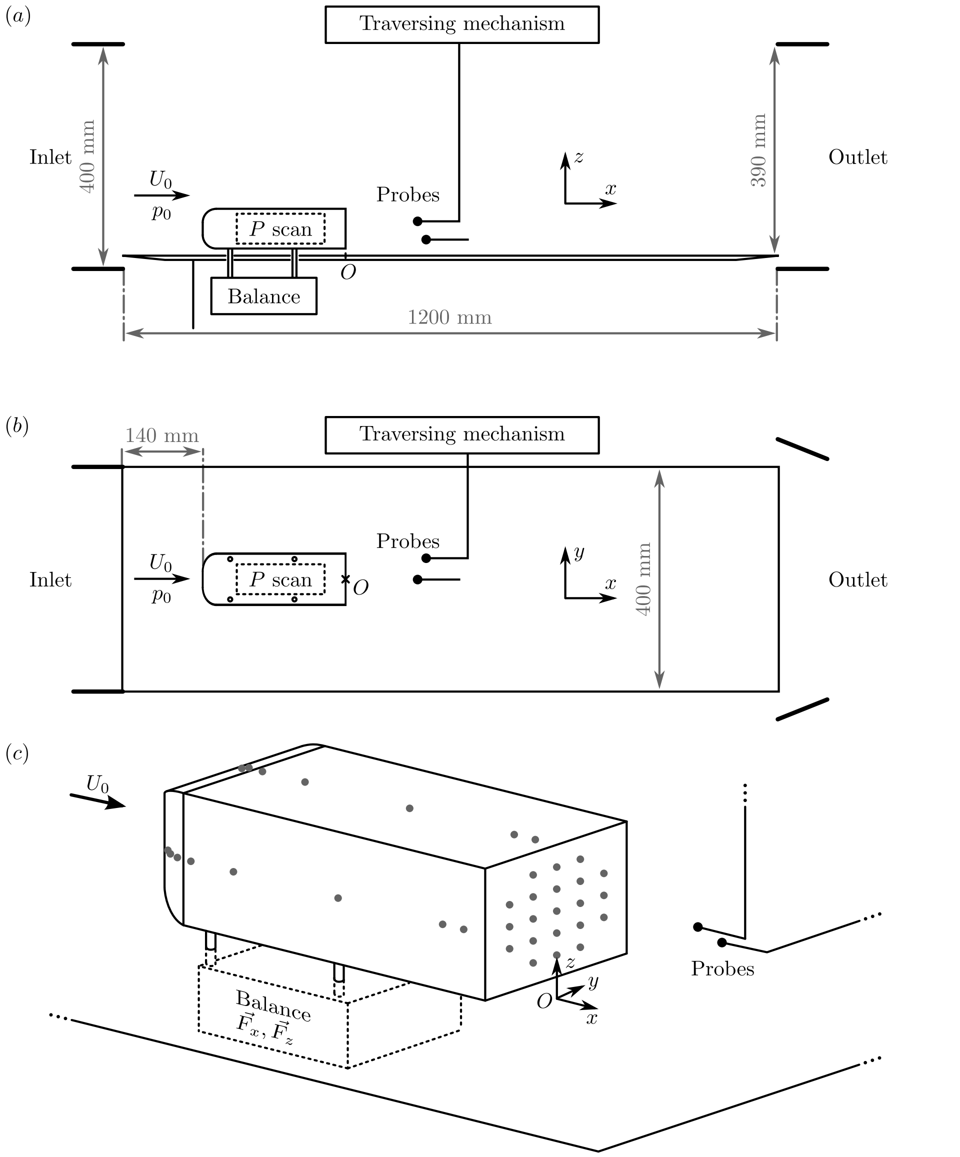

FIGURE 1. Experimental set-up: side view (a), top view (b) and perspective view (c); O sets the origin of the coordinate system.

curate when the flow is aligned with the probe. However it is used as a qualitative indicator of pressure in the entire wake to locate the low pressure regions. A three-dimensional mapping of the static pressure is obtained moving the probe in the region $(x^*, y^*, z^*) \in [0.14; 3] \times [-0.83; 0.83] \times [0.07; 1.67]$ by steps of 0.14 in the streamwise direction and of 0.07 in the crossflow directions.

2.3. *Force measurements*

Drag and lift, respectively F_x and F_z, are obtained using a bidirectional strain balance. The dimensionless coefficient C_i of the aerodynamic force in the i direction is defined according to (2.1) using $S = 7.19\ 10^{-3}$ m^2 the projected area of the geometry in a crossflow plane.

$$C_i = \frac{F_i}{\frac{1}{2}\rho S {U_0}^2}, \tag{2.1}$$

with $i \in \{x, y, z\}$.
The pressure measurements enable the origins of the aerodynamic forces to be clarified. The pressure contribution to the aerodynamic force in the i direction (denoted by C_{ip}) is estimated by integration of the pressure projected in the considered direction as defined in (2.2). The precision is limited especially for the measurement of the lift and lateral forces since the pressure distribution is assumed independent of y on the top and bottom faces and independent of z on the lateral faces.

$$C_{ip} = \frac{1}{S} \int_{body} C_p\, \vec{e_i} \cdot \vec{ds}, \tag{2.2}$$

with $C_p = \frac{P - P_0}{\frac{1}{2}\rho {U_0}^2}$ and $i \in \{x, y, z\}$.

2.4. *Velocity measurements*

2.4.1. *Particle Image Velocimetry*

Wake analyses are made from Particle Image Velocimetry (PIV). The system is comprised of a DANTEC dual pulse laser (Nd:YAG, 2×135 mJ, 4 ns) and two DANTEC CCD cameras (FlowSense EO, 4 Mpx). The set-up acquires image pairs at a rate of 10 Hz; each acquisition records 2000 image pairs. The interrogation window size is 32×32 pixels with an overlap of 25%. The bi-dimensional velocity measurements are performed in planes $y^* = 0$ and $z^* = 0.6$ and stereo-PIV enables to measure the three components of the velocity in planes $x^* = 1$ and $x^* = 2$. The 32×32 pixels of the interrogation window correspond to physical sizes of 2.5×2.5 mm in the plane $y^* = 0$, 1.6×1.6 mm in the plane $z^* = 0.6$ and 2.4×2.4 mm in the planes $x^* = 1$ and $x^* = 2$.
The mean velocities and the Reynolds stresses are measured from the valid vectors of the instantaneous velocity fields; these statistics are taken into account only when more than 1500 valid vectors are obtained from the 2000 measurements.

2.4.2. *Hot-wire probes*

To get the unsteady characteristics of the flow, 1D hot-wire probes are used. The wire probes are from DANTEC (hot-wire type 55P15, support type 55H22) and use an overheat ratio of 1.5; they are connected to two DISA55 hot wire anemometry measurement units. These probes mounted on the displacement systems record the velocity in the wake at a sampling frequency of 1 kHz. Velocity signals are recorded during several minutes and power spectra are averaged over windows of 1 s, 2 s or 10 s. This averaging over windows is denoted by "$\langle ... \rangle_W$". $\xi_F(f)$ standing for the Fourier transform of the function ξ evaluated at the frequency f and $\overline{\xi}(f)$ for its complex conjugate, the power spectal density (PSD) is calculated from the signal $a(t)$ as defined in (2.3). Autopower spectra are then obtained up to 500 Hz with a resolution of 0.1, 0.5 or 1 Hz.

$$PSD(f) = \langle a_F(f)\ \overline{a_F}(f) \rangle_W. \tag{2.3}$$

Cross correlations between two hot-wire probes at different locations are also performed: the coherence r_F and phase ϕ between the signals $a(t)$ and $b(t)$ are the modulus and the argument of γ defined in (2.4).

$$\gamma = \frac{\langle a_F(f)\ \overline{b_F}(f)\rangle_W}{\sqrt{\langle |a_F(f)|^2\rangle_W \langle |b_F(f)|^2\rangle_W}} = r_F(f)e^{i\phi(f)}. \tag{2.4}$$

3. Results

3.1. *Mean properties of the flow*

The mean flow over this geometry can be seen in figure 2; it presents different separations. First, a boundary layer detachment occurs on the four faces at the end of the nose due to the adverse pressure gradient imposed by the geometry. Indeed, the pressure measurements in the planes $y^* = 0$ and $z^* = 0.67$ (see figure 3*a*–*b*) locate the separated regions through characteristic plateaus on the body roughly for $-3.5 < x^* < -3.0$ on the four faces. Reattachment, associated with the pressure recovery on the surface, is then reported at $x^* \approx -3.0$ on the sides and top faces but slightly before on the bottom face. This absence of symmetry is due to the ground, its presence does not prevent the boundary layer detachment on the bottom face of the body but makes the flow reattach sooner. These flow separations are also reported at very large Reynolds number as observed in appendix A and in various experiments or numerical simulations (Spohn & Gilliéron 2002; Krajnović & Davidson 2005; Franck *et al.* 2009).
The measurement of the velocity profiles at the trailing edge is performed to know whether the boundary layers are turbulent or not before separation and also to provide information on their characteristic thickness. The results are presented in figure 4; the separations at the end of the forebody induce important losses of momentum beyond the boundary layer at the trailing edge. The levels of fluctuating velocities also remain important due to these separations except in the case of the bottom face (see figure 4*c*) where the ground proximity limits the detachment. The peaks of fluctuating velocities near the surface indicate that the boundary layers are fully turbulent at the trailing edge but the absence of constant velocity far from the surface prevents the use of classical definitions of characteristic thicknesses. However, considering the size of the region of intense vorticity near the body, the normalized initial heights of shear layers that separate at the trailing edge are respectively 0.026, 0.025 and 0.017 for the top, side and bottom faces with a precision of 0.03.

The blunt trailing edge imposes a massive separation of the flow at the base. The recirculation region characterized in figures 2(*a*)–(*c*) extends up to $x^* = 1.47$. The crossflow-PIV measurements at $x^* = 1$ (see figure 2*c*) show that the recirculation region preserves roughly the shape of the rectangular trailing edge: the geometry of the contour ${U_x}^* = 0$ seems to result from the equal growth of the mixing layer from the separation at $x^* = 0$, at least on the top and side faces. The recirculation bubble then closes in the plane $z^* = 0.6$ with two saddle points ($x^* = 1.46$ and $y^* \approx \pm 0.17$). Despite the ground presence, the mean velocities at the center of the recirculation region remain oriented along the x direction. Thus, these PIV measurements emphasize the time-averaged vision of the toric recirculation organization which is also observed through the pressure measurements in the wake.
Figures 5(*a*)–(*b*) show the contours of pressure in the planes $y^* = 0$ and $z^* = 0.67$. The minima of pressure in the wake are reported inside the recirculation region, near the separatix in the plane $y^* = 0$. These locations correspond to the center of the time-averaged recirculation structures visible in figure 2(*a*)–(*b*). The three-dimensional mapping of the static pressure highlights the shape of the region in the recirculation bubble where the

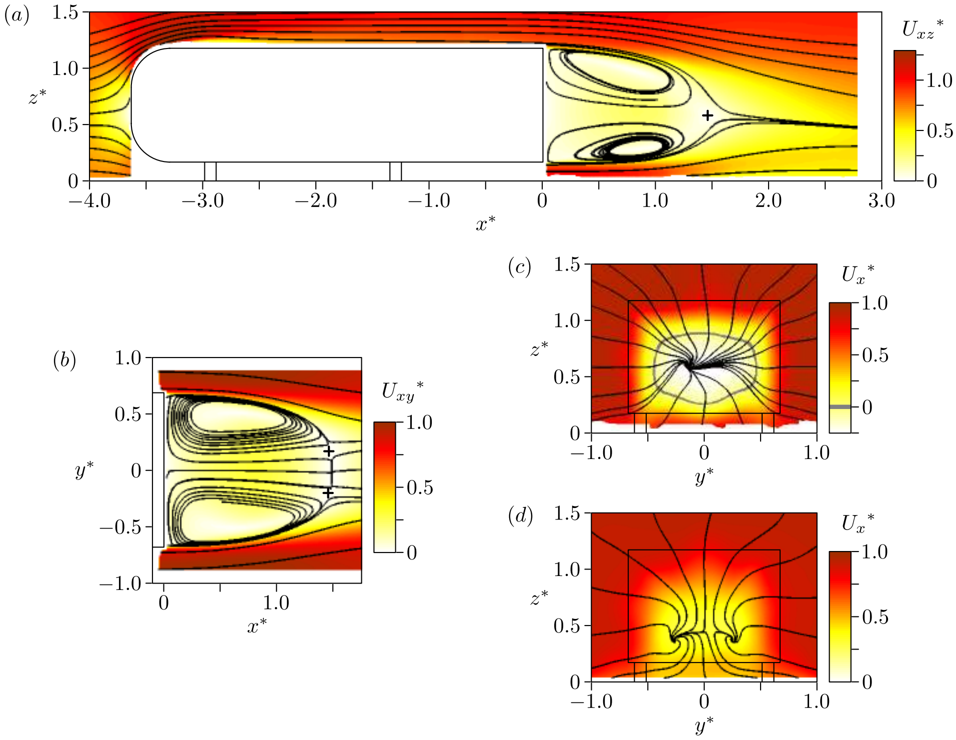

FIGURE 2. Streamlines colored by velocity in the plane $y^* = 0$ (a), $z^* = 0.6$ (b), $x^* = 1$ (c) and $x^* = 2$ (d). Crosses are saddle points.

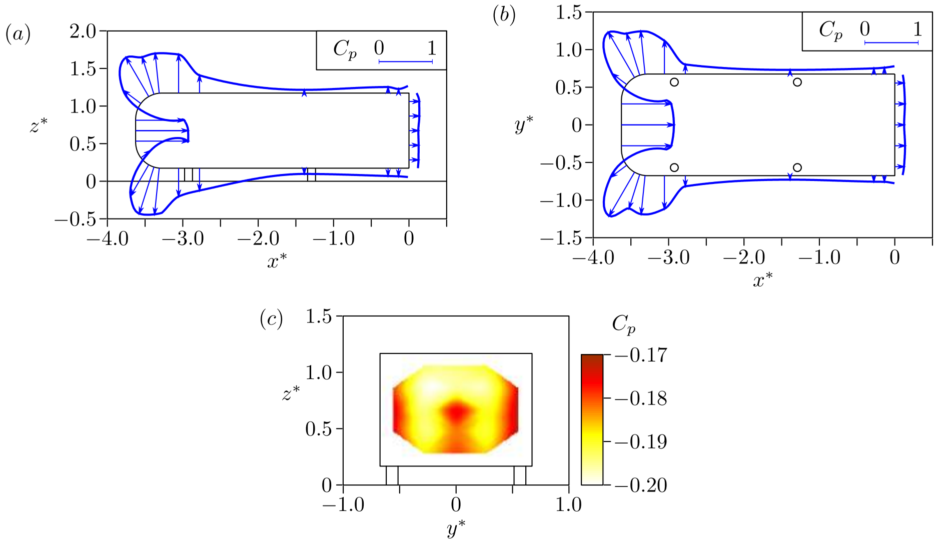

FIGURE 3. Distribution of C_p on the body in the planes $y^* = 0$ (a), $z^* = 0.67$ (b) and on the base (c). Arrows locate pressure taps.

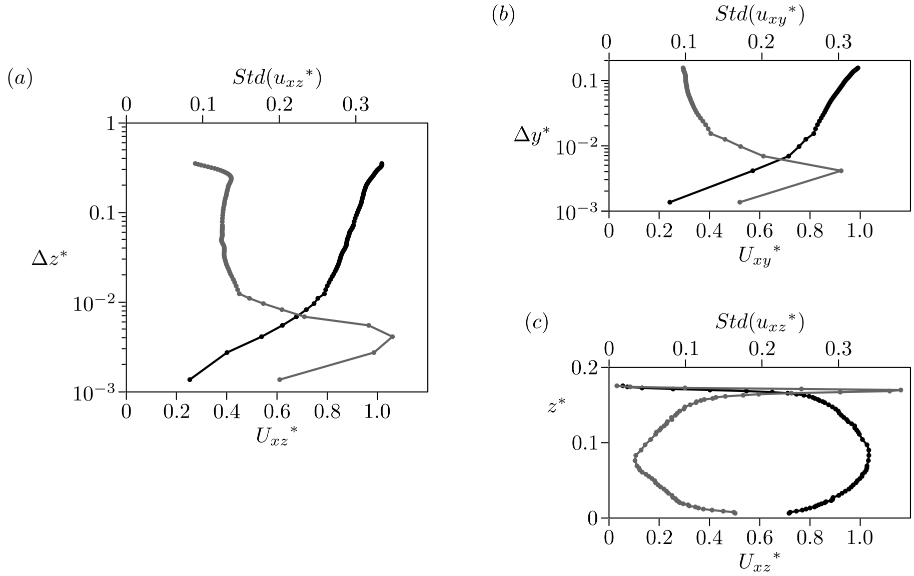

FIGURE 4. Mean (black line, bottom axis) and fluctuating (gray line, top axis) velocity profiles of the boundary layers at $x^* = 0$ from the top face at $y^* = 0$ (a), a side face at $z^* = 0.67$ (b) and the bottom face at $y^* = 0$ (c). Δy and Δz are the gaps between the hot-wire probe and the surface.

pressure is lowest at $x^* \approx 0.6$ (see figure 5c). Downstream of the recirculation region, the pressure coefficient reaches positive values associated with the change of the streamlines curvature. The adverse pressure gradient is particularly intense on the ground between $x^* = 1$ and $x^* = 2$. It induces significant losses of momentum on the ground downstream of the body (see figures 2a and 2d). Boundary layer separation on the ground in this region is not observed but may occur for smaller ground clearances like in the experiments of Ruiz *et al.* (2009).

The effects of the low pressure region in the recirculating flow can be seen on the afterbody. The pressure on the base is measured approximately constant around $C_{pb} = -0.185$ as visible in figure 3(c) and the slight variations reflect the region of low pressure presented in figure 5. The value of the drag measured with the balance is $C_x = 0.274 \pm 0.003$; it is slightly bigger than the drag coefficient of 0.250 presented in Ahmed *et al.* (1984) but this value is consistent with the other results reported in literature, usually between 0.26 and 0.32. Considering the distributions of pressure shown in figure 3, the pressure component of the aerodynamic forces can be estimated as described in section 2.3, the different contributions are given in table 1. The dominant part of pressure drag ($C_{xp} \approx 0.75\, C_x$) mostly associated with the low base pressure is also in good agreement with the results published by Ahmed *et al.* (1984). The negative sign of C_z is related to the pair of counter-rotating vortices observed through the streamlines in the crossflow plane at $x^* = 2$ (see figure 2d). Similarly, $C_{yp} \approx 0$ is coherent with the symmetry of both the geometry and the flow.

The PIV results equally allow the measurements of the Reynolds stresses in the different planes. Figure 6 presents the components $\langle {u'_x}^2 \rangle$, $\langle {u'_z}^2 \rangle$ and $\langle u'_x u'_z \rangle$. They are particularly intense at the forebody separation and they are convected to the top trailing edge as previously seen in the boundary layer profiles. The ground induces a slight asym-

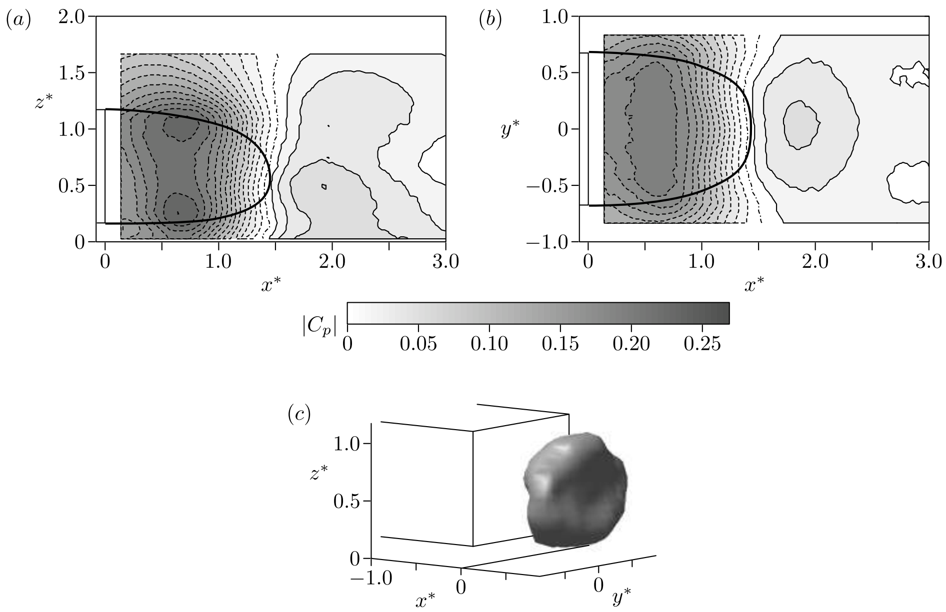

FIGURE 5. Contours of static pressure in the plane $y^* = 0$ (a) and $z^* = 0.67$ (b); continuous and dashed lines are respectively positive and negative values, contour 0 is dotted-dashed line, contour intervals are 0.02. The thick black line represents the separatrix of the mean flow. (c) Isosurface of pressure $C_p = -0.2$ in the recirculation region.

C_x	=	0.274	±	0.003
C_z	=	−0.038	±	0.008
C_{xp}	=	0.206	±	0.005
C_{yp}	=	0.006	±	0.015
C_{zp}	=	−0.080	±	0.015
C_{pb}	=	−0.185	±	0.003

TABLE 1. Aerodynamic forces on the body and their pressure components.

metry in the z direction. After the massive separation at $x^* = 0$, the mixing layers develop mostly toward the recirculation region and the highest values of normal and shear stresses are measured on the separatrix. The intensities and spatial distribution of the Reynolds stresses in the plane $y^* = 0$ are in good agreement with the measurements of Khalighi *et al.* (2001). The maximum values measured in the wake are detailed in table 2 however it is worth mentioning that the maximum of the streamwise Reynolds stresses is measured in the mixing layer from the forebody detachment: $\langle {u'_x}^{*2} \rangle = 0.23$ at $(x^* = -3.06, z^* = 1.24)$. Similar results are obtained in the plane $z^* = 0.6$ in figures 7(a) and (c). Nevertheless, contrary to the results presented in figure 6(b), the highest values of $\langle {u'_y}^2 \rangle$ are measured at $y^* = 0$ upstream of the end of the recirculation region (see figure 7b). Finally, the values of the Reynolds stresses in the plane $x^* = 1$ in figure 8 confirm that the dominant component is the normal streamwise stress $\langle {u'_x}^2 \rangle$ and that the shear stresses from the top / bottom faces are more intense than from the lateral ones. The Reynolds stresses from stereo PIV in the plane $x^* = 1$ (figure 8) are slightly under-evaluated compared to the ones from bi-dimensional PIV in the planes $y^* = 0$ and $z^* = 0.6$ (figures 6 and 7) but their spatial distributions are coherent.

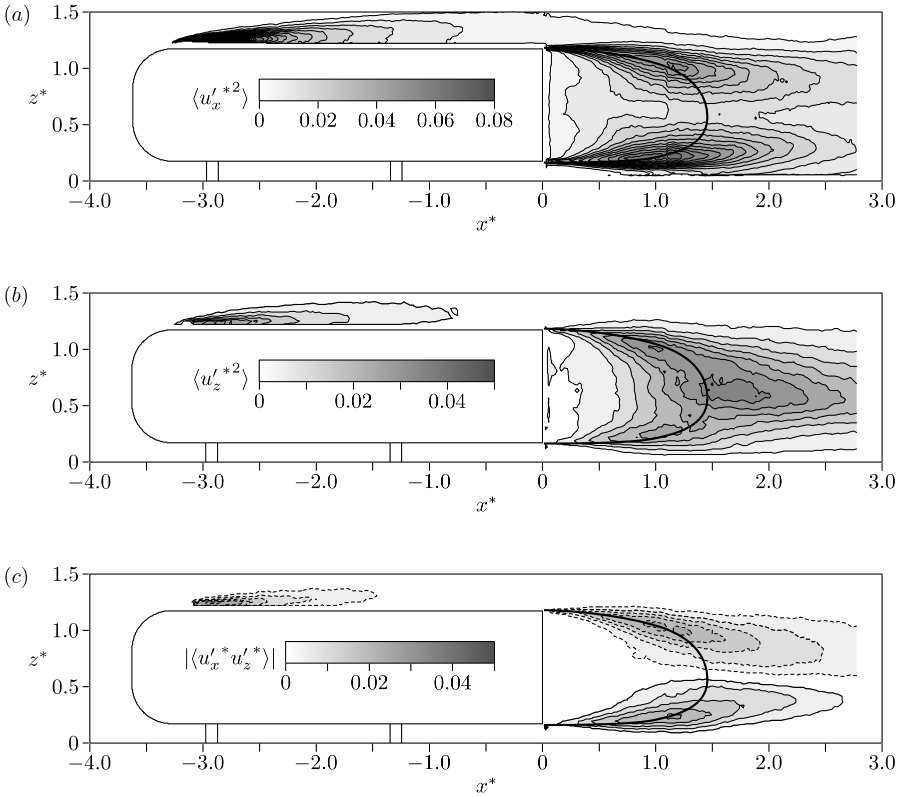

FIGURE 6. Contours of Reynolds stresses in the plane $y^* = 0$: $\langle {u'_x}^{*2} \rangle$, (*a*); $\langle {u'_z}^{*2} \rangle$, (*b*); $\langle {u'_x}^* {u'_z}^* \rangle$, (*c*). Continuous and dashed lines are respectively positive and negative values, contour intervals are 0.005, contour 0 is not plotted. The thick black line represents the separatrix of the mean flow.

These different stresses contribute to the equilibrium of the recirculation region in the x direction. Indeed, the recirculation bubble of the mean flow is a force balance of the pressure forces, the shear stresses and the normal stresses. Balachandar *et al.* (1997) analyzed this equilibrium in the wake of cylinders. In the present case, when the viscous forces are neglected, the momentum conservation on the contour $\partial\Omega$ delimited by the base of the body and the contour of the bubble is studied; $\partial\Omega$ is assumed hermetic which may be a rough approximation in three-dimensional flows. The equilibrium in the x direction is then given by

$$\int_{\partial\Omega} \rho \langle u'_x u'_i \rangle n_i \, \mathrm{d}s + \int_{\partial\Omega} P n_x \, \mathrm{d}s = 0, \tag{3.1}$$

with $\vec{n} = n_i \vec{e_i}$ normal to $\partial\Omega$. This leads to

$$\int_{\mathrm{Base}} C_p \, \mathrm{d}s = 2 \int_{\mathrm{Bubble}} \langle {u'_x}^* {u'_i}^* \rangle n_i \, \mathrm{d}s + \int_{\mathrm{Bubble}} C_p n_x \, \mathrm{d}s. \tag{3.2}$$

The terms of the relationship (3.2) cannot be estimated with a reasonable precision from these measurements but the equilibrium shows the critical influence of the Reynolds stresses on the base drag. The energy of the fluctuations of velocities is associated with the turbulent evolution of the flow but also with some coherent motions of the fluid which are depicted in section 3.2.

	Present study	Khalighi *et al.* (2001)
$\max_{x^*>0} \langle {u'_x}^{*2} \rangle$	0.069 at ($x^* = 1.18, z^* = 0.22$)	0.08 at $x^* = 1.5 \pm 0.5$ (bottom mix. lay.)
$\max_{x^*>0} \langle {u'_z}^{*2} \rangle$	0.038 at ($x^* = 1.67, z^* = 0.61$)	–
$\max_{x^*>0} \lvert\langle {u'_x}^{*} {u'_z}^{*} \rangle\rvert$	0.027 at ($x^* = 1.24, z^* = 1.00$)	0.019 at $x^* = 2.0 \pm 0.5$ (top mix. lay.)

TABLE 2. Maximum values and locations of the Reynolds stresses in the plane $y^* = 0$.

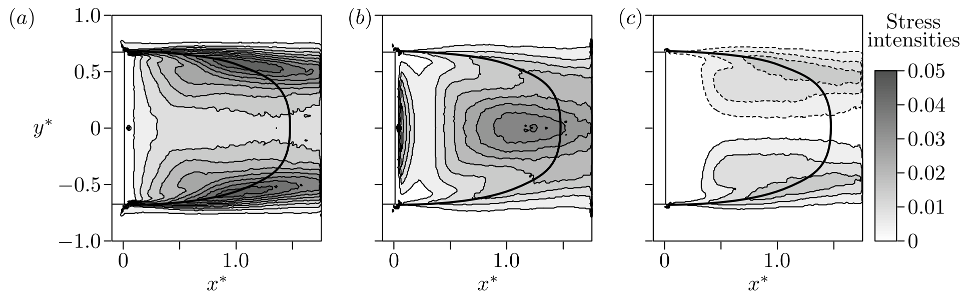

FIGURE 7. Contours of Reynolds stresses in the plane $z^* = 0.6$: $\langle {u'_x}^{*2} \rangle$, ($a$); $\langle {u'_y}^{*2} \rangle$, ($b$); $\langle {u'_x}^{*} {u'_y}^{*} \rangle$, ($c$). Continuous and dashed lines are respectively positive and negative values, contour intervals are 0.005, contour 0 is not plotted. The thick black line represents the separatrix of the mean flow.

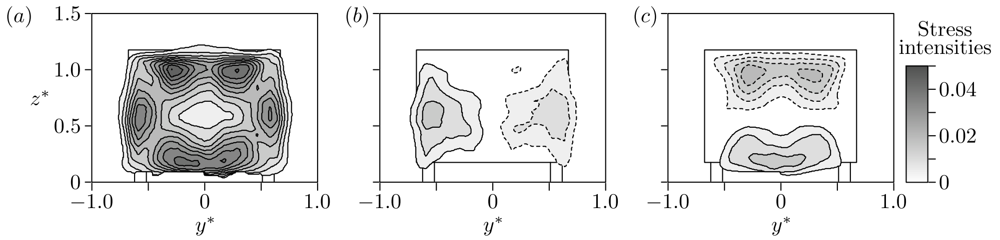

FIGURE 8. Contours of Reynolds stresses in the plane $x^* = 1$: $\langle {u'_x}^{*2} \rangle$, ($a$); $\langle {u'_x}^{*} {u'_y}^{*} \rangle$, ($b$); $\langle {u'_x}^{*} {u'_z}^{*} \rangle$, ($c$). Continuous and dashed lines are respectively positive and negative values, contour intervals are 0.005, contour 0 is not plotted.

3.2. *Dynamics of the wake*

The autopower spectra of hot-wire probe signals in the wake highlight different characteristic frequencies. Figure 9(a) shows the autopower spectra at the points A and B respectively located at $(2.5, 0, 0.9)$ and $(2.5, 0.5, 0.6)$, *i.e.* downstream of the top and the lateral mixing layers. Peaks of energy are reported at 35.4 Hz and 48.4 Hz with a precision of 0.2 Hz, the corresponding Strouhal numbers ($\mathrm{St} = fH/U_0$) are 0.127 and 0.174. In addition, the probe located at B measures an important energy in the low frequency domain. This phenomenon is clear in figure 9(b): long time evolutions (over 1 s) are observed on the velocity measurement at B. These coherent dynamics of the wake, one with long time evolutions, the others at higher frequencies, are respectively depicted in sections 3.2.1 and 3.2.2.

3.2.1. *Bi-stability*

From the local measurement of the velocity at B presented in figure 9(b), a bi-stable behavior seems to be detected in the wake, this phenomenon is confirmed using global quantities of the wake. As it has long time evolutions, it can be analyzed using the PIV

FIGURE 9. Autopower spectra (a) and sample time evolution (b) of the velocity signals recorded at $A(2.5, 0, 0.9)$ (continuous black line) and $B(2.5, 0.5, 0.6)$ (dashed gray line) from hot-wire measurements.

measurements at 10 Hz. In the plane $x^* = 1$, the barycenter of momentum deficiency is considered as a parameter of order through the quantities ${y_W}^*$ and ${z_W}^*$ defined as:

$$ {y_W}^* = \frac{\int y^* \cdot (1 - {u_x}^*)\,\mathrm{d}s}{\int (1 - {u_x}^*)\,\mathrm{d}s}, \tag{3.3} $$

and

$$ {z_W}^* = \frac{\int z^* \cdot (1 - {u_x}^*)\,\mathrm{d}s}{\int (1 - {u_x}^*)\,\mathrm{d}s}; \tag{3.4} $$

with a domain of integration limited to ${u_x}^* < 1$.

Figure 10(a) presents a PIV snapshot of the streamwise velocity in the plane $x^* = 1$ and the associated position of the barycenter of the momentum deficiency at ${y_W}^* = 0.043$ and ${z_W}^* = 0.575$. The time evolution of the positions ${y_W}^*$ and ${z_W}^*$ over the 200 s of the PIV measurements (2000 snapshots recorded at 10 Hz) are plotted in figure 10(b) and 10(c) respectively. The associated probability densities clearly highlight one preferred position in the z direction but two different positions in the y direction centered on ${y_W}^* = \pm 0.06$. The states are denoted by #P for the one associated with a positive value of ${y_W}^*$ and #N for the one with a negative value of ${y_W}^*$. Similar probability densities with two preferred positions are also obtained from the analyses of the snapshots in the plane $x^* = 2$ and the $z^* = 0.6$. Therefore, the two preferred states of the wake can be discriminated through the distributions of velocity in the wake. Conditional averaging over the sign of ${y_W}^*$ enables the extraction of the asymmetric topologies from the PIV measurements presented in figure 2. The results corresponding to the state #P are displayed in figure 11. Figure 11(a) presents the asymmetric flow in the plane $z^* = 0.6$. As in the experiments of Grandemange *et al.* (2012b), there is only one saddle point left off the streamwise axis and the mean recirculation flow is diagonal. Figures 11(b)–(c) show the flow in the crossflow planes $x^* = 1$ and $x^* = 2$ with a clear asymmetry.

This topology #P also induces asymmetric Reynolds stress distributions in the planes $z^* = 0.6$ (figure 12) and $x^* = 1$ (figure 13). The $y^* = 0$ reflectional symmetry is lost, the activities of the mixing layer is mostly concentrated on the side where wake is oriented. On the other hand, figure 13 shows that the top / bottom mixing layer characteristics are almost independent of the state of the wake.

As the two states are associated with a diagonal recirculating flow, they are also characterized by base pressure distributions which are asymmetric in the y direction (Grandemange *et al.* 2012b). The states #P and #N can then be studied through pressure measurements since the sampling frequency of 1 Hz does not limit the analyses of this long time evolution behavior. Figure 14 presents sample evolutions and the probability distributions of the pressure gradient in the y and z directions on the base at $y^* = 0$ for measurements performed over 10^4 s. Figure 14(b) shows that the most probable value of the pressure gradient in the z direction is close to its mean value which is slightly negative

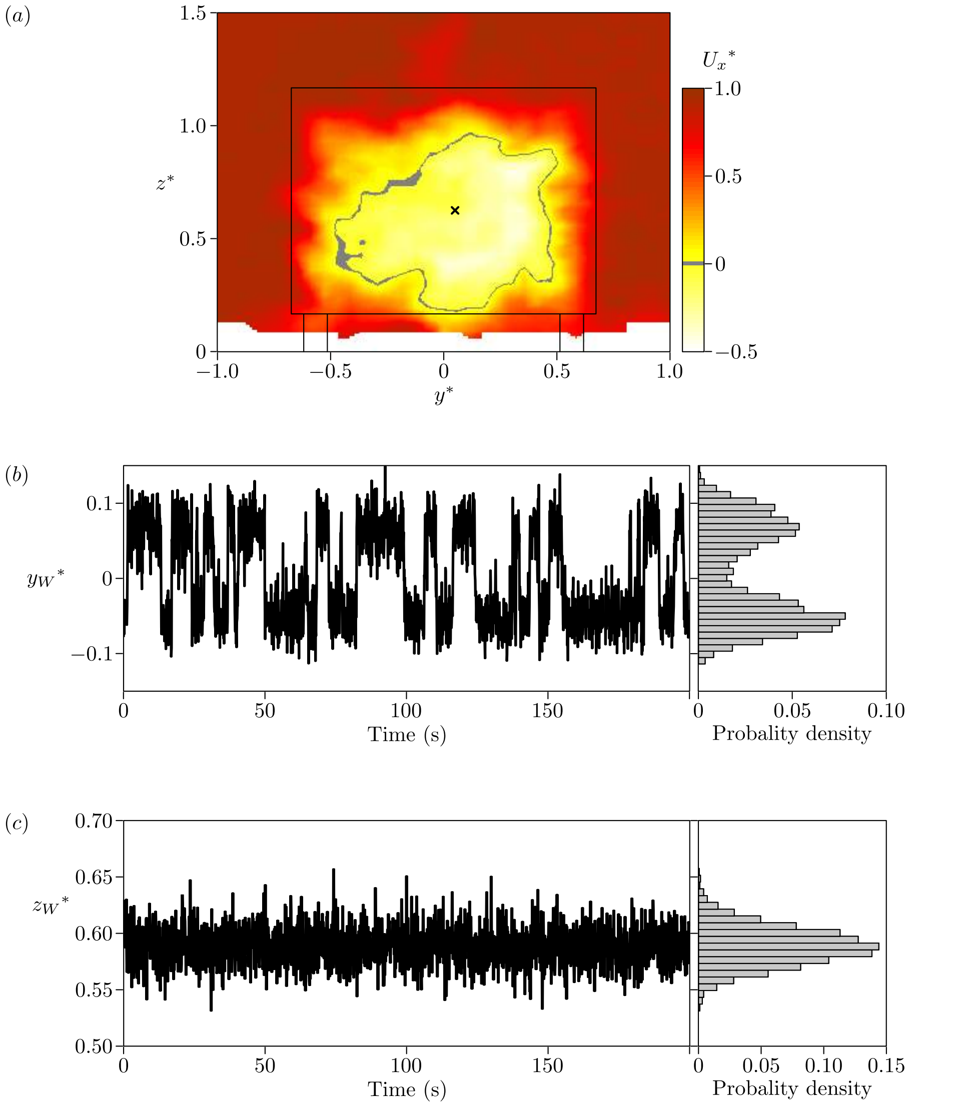

FIGURE 10. (a) Snapshot of streamwise velocity in the plane $x^* = 1$; $\times$, barycenter of momentum deficiency located at $y_W{}^* = 0.043$ and $z_W{}^* = 0.575$. (b) Time evolution of the barycenter of momentum deficiency in the y direction and associated probability distribution. (c) Same as (b) in the z direction.

as expected from figure 3(c). On the contrary, the histogram in figure 14(a) is balanced but the two states are clearly visible. The states are associated with $\frac{\partial c_p}{\partial y^*} = \pm 0.17$ and the state #P corresponds to the one with a positive gradient and #N to the one with a negative gradient. 5% of the measurements correspond to $|\frac{\partial c_p}{\partial y^*}| < 0.1$ but they are likely to be cases of shift from one asymmetric state to another during a pressure measurement; this interpretation is consistent with the equiprobability of these values of base pressure gradient. Conditional averaging of the pressure is then performed using the sign of $\frac{\partial c_p}{\partial y^*}$ as a topology indicator.

Figure 15(a) shows the distribution of pressure on the body in the plane $z^* = 0.67$. The asymmetric distributions related to the two preferred values of pressure gradient in

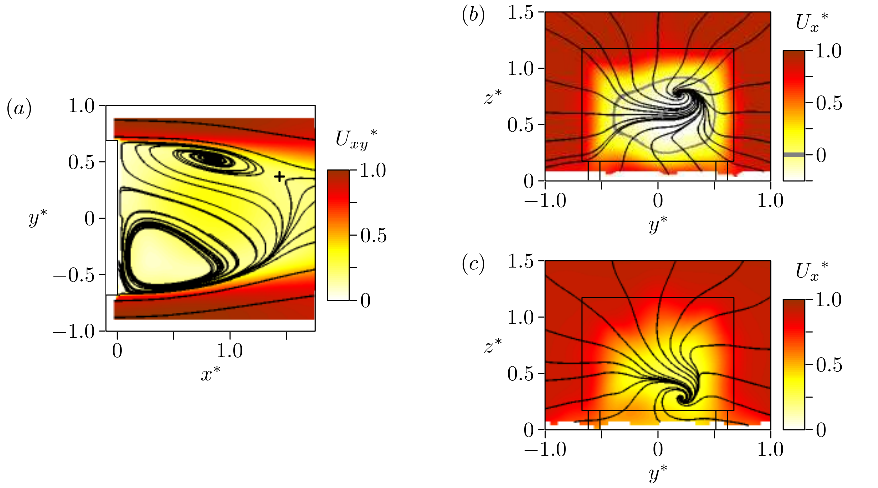

FIGURE 11. Streamlines colored by velocity corresponding to state #P in the planes $z^* = 0.6$ (*a*), $x^* = 1$ (*b*) and $x^* = 2$ (*c*). Crosses are saddle points.

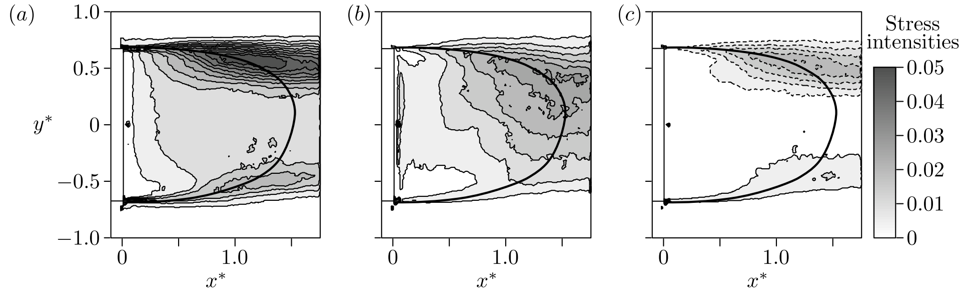

FIGURE 12. Contours of Reynolds stresses in the plane $z^* = 0.6$ of the wake in the #P state: $\langle {u'_x}^{*2} \rangle$, (*a*); $\langle {u'_y}^{*2} \rangle$, (*b*); $\langle {u'_x}^* {u'_y}^* \rangle$, (*c*). Continuous and dashed lines are respectively positive and negative values, contour intervals are 0.005, contour 0 is not plotted. The thick black line represents the separatrix of the mean flow of the #P state.

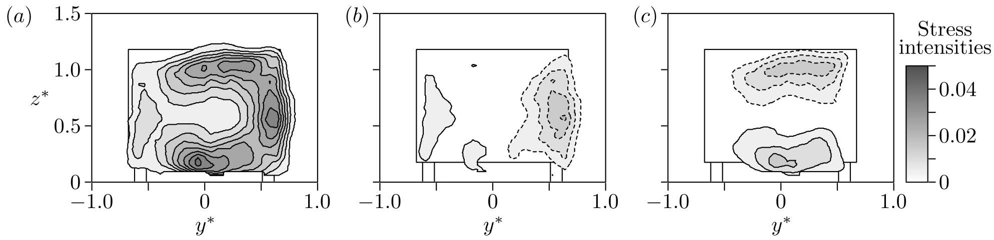

FIGURE 13. Contours of Reynolds stresses in the plane $x^* = 1$ of the wake in the #P state: $\langle {u'_x}^{*2} \rangle$, (*a*); $\langle {u'_x}^* {u'_y}^* \rangle$, (*b*); $\langle {u'_x}^* {u'_z}^* \rangle$, (*c*). Continuous and dashed lines are respectively positive and negative values, contour intervals are 0.005, contour 0 is not plotted.

the y direction in the middle of the base are clearly visible but only on the afterbody. The coexistence of these two states leads to the mean symmetric pressure distribution plotted in figure 3. These distributions are independent of the state for $x^* < -1$ which indicates that the stagnation point on the forebody is fixed. Thus the bi-stable behavior is the result of neither low frequency oscillations of the free flow direction nor some wind tunnel modes.

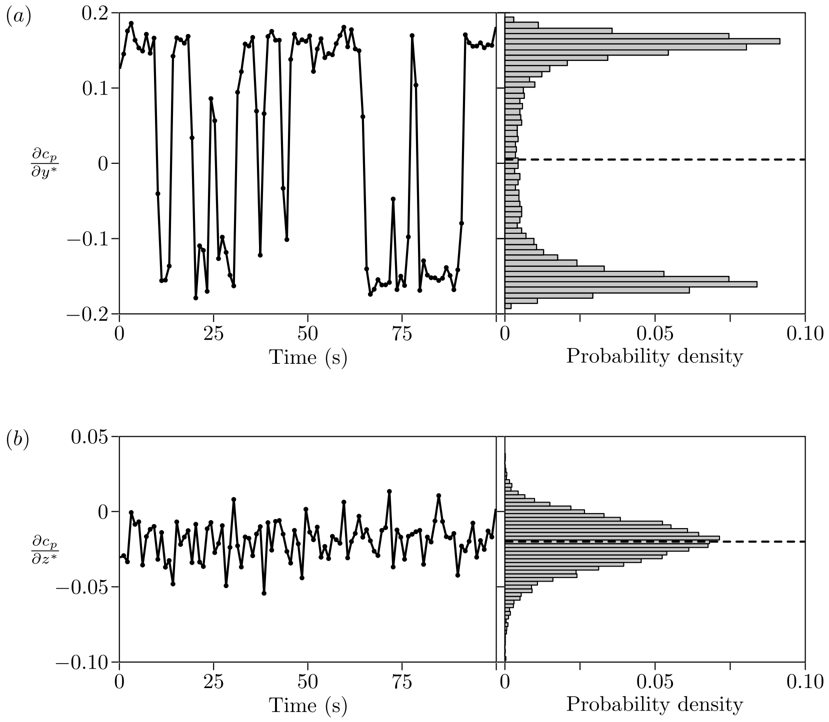

FIGURE 14. Sample time evolution and probability distribution of the base pressure gradient in the y direction (a) and in the z direction (b) at $y^* = 0$; dashed lines are mean values.

Using the base pressure gradient as an indicator, the distribution of base pressure can be obtained for the state #P where $\frac{\partial c_p}{\partial y^*} > 0$. The results presented in figure 15(b) show that the asymmetry is a global characteristic of the pressure on the base: it ranges from $C_p = -0.24$ to $C_p = -0.12$ and presents much larger variations than the results displayed in figure 3(c). It is then important to note that the view of a toric recirculation organization is not pertinent as it does not reflect the topology of the flow.
Besides, the asymmetric distributions of pressure presented in figure 15(a) are associated with lateral forces that counterbalance in average. The pressure forces of the asymmetric states in the y direction are evaluated at $C_{yp} = \pm 0.021$ with a precision of 0.015; it corresponds to the difference of the pressure on the side of the body for $-1 < x^* < 0$. This force in the y direction is associated with the wake asymmetry visible in figure 11(c). It must equally be correlated with some circulation around the body. The difference in streamwise pressure gradient on the sides of the body is linked to distinct boundary layer characteristics that are studied in the following paragraph.

The boundary layer velocities presented in figure 4(b) can equally be analyzed regarding the bi-stability. An example of velocity signal in the boundary layer is displayed in figure 16(a). Like in figure 9(b), a bistable behavior seems present but is not directly visible in the probability distribution. When the same velocity signal is filtered using an average filter over windows of 0.5 s as displayed in figure 16(b), the probability distribution shows two peaks corresponding to the two topologies #P and #N. For each point of measurement in the boundary layer profile, this method enables the discrimination of the two topologies. Conditional averaging then gives access to the boundary layer profiles of each state presented in figure 17. The characteristic heights of the boundary layers of the

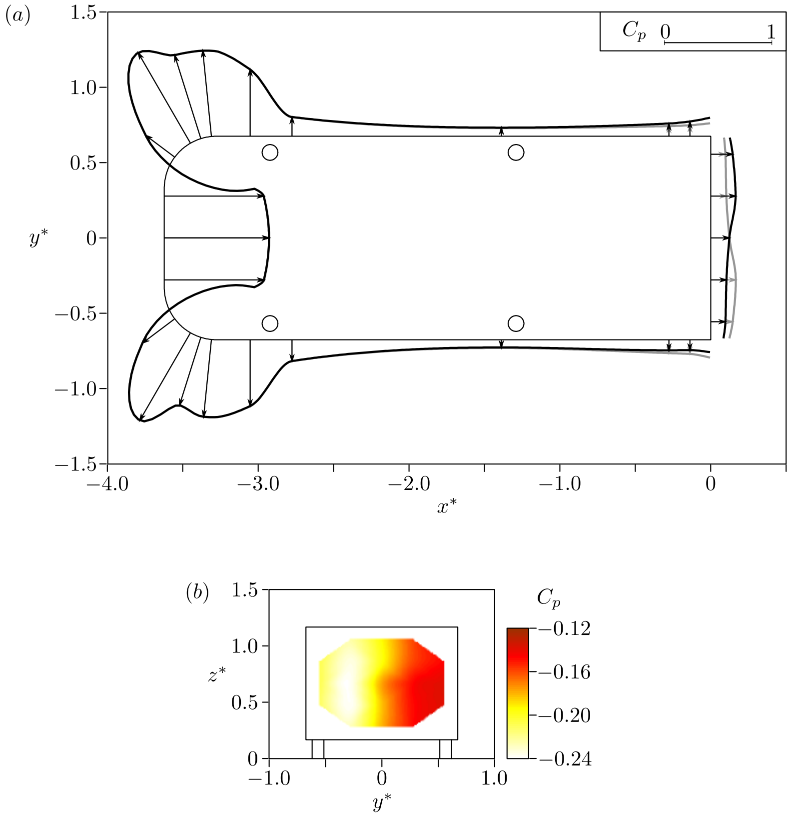

FIGURE 15. (*a*) Pressure distribution of the states #N (black line) and #P (grey line) on the body in the plane $z^* = 0.67$. Arrows locate pressure taps. (*b*) Pressure distribution of the state #P on the base.

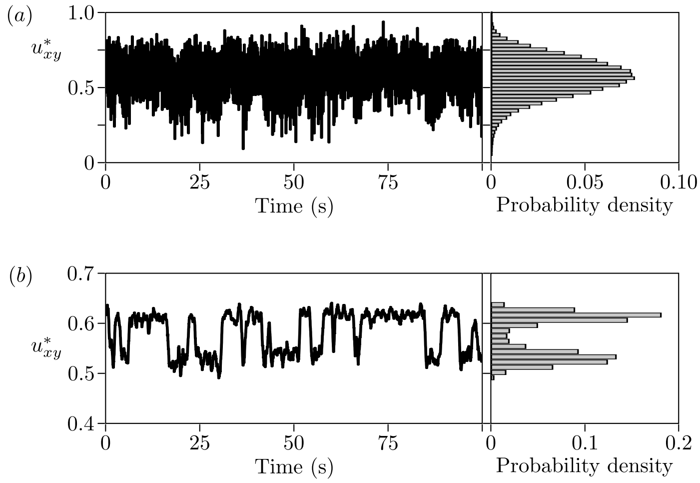

FIGURE 16. Sample time evolution of the velocity in the lateral boundary layer at the trailing edge and associated probability distribution: raw measurement (*a*) and filtered signal using an averaging filter over a window of 0.5 s (*b*).

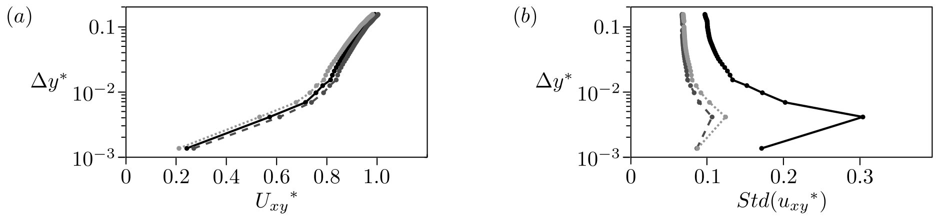

FIGURE 17. Mean (a) and fluctuating (b) velocity profiles of the boundary layers from the middle of the side face ($y^* > 0$) at the trailing edge for the symmetric mean flow (continuous line), the state #N (dashed line) and the state #P (dotted line). Δy is the gap between the probe and the surface.

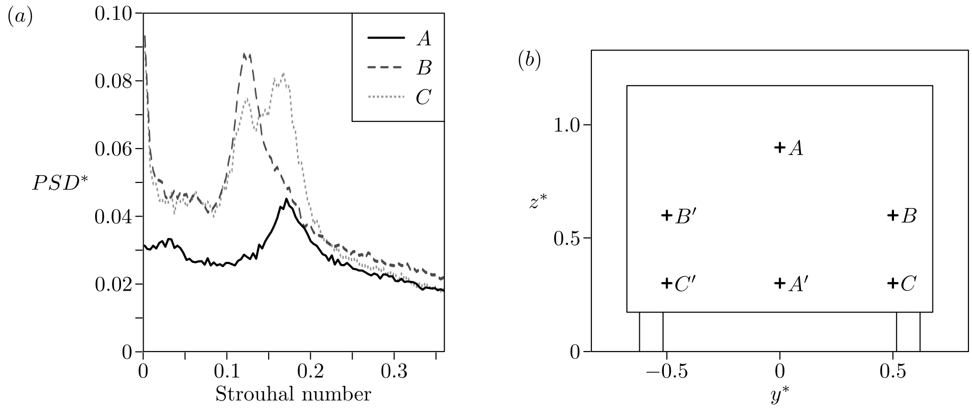

FIGURE 18. (a) Autopower spectra in the wake at $A(2.5, 0, 0.9)$ (continuous line), $B(2.5, 0.5, 0.6)$ (dashed line) and $C(2.5, 0.5, 0.3)$ (dotted line). (b) Locations of the hot-wire probe position A, A', B, B', C and C' in the crossflow plane $x^* = 2.5$ used in the analyses of the oscillating global modes.

two states are similar and measured at 0.024 for the faster profile and 0.026 for the slower one with a precision of 0.003. The profiles of velocity fluctuations indicate that the two boundary layers are turbulent which confirms that the bi-stability is neither associated with an intermittent boundary separation on the nose nor dependent on its laminar or turbulent characteristic at the trailing edge. The difference in the levels of velocity fluctuations between the mean symmetric flow and the asymmetric states in figure 17(b) is due to the contribution of the bi-stability to the fluctuations from the changes of mean velocity visible in figure 17(a).

3.2.2. *Oscillating global modes*

In addition to the low frequency evolutions, the autopower spectra at $A(2.5, 0, 0.9)$ and $B(2.5, 0.5, 0.6)$ reveal two peaks of energy at Strouhal numbers 0.127 and 0.174 (see figure 18a). These characteristic frequencies are denoted by f_1 and f_2 respectively and the Strouhal numbers are St_1 and St_2. As in the experiments of Kiya & Abe (1999), depending on the hot-wire position, one or both frequencies are measured. The recurrent probe positions A, A', B, B', C and C' used in the plane $x^* = 2.5$ are presented in figure 18(b).

To examine the envelops of these two modes, autopower spectra are studied depending on the position of the hot-wire probe in the wake. The spectra in the plane $z^* = 0.6$ are shown in figure 19 for different downstream locations. Only the St_1 mode is reported.

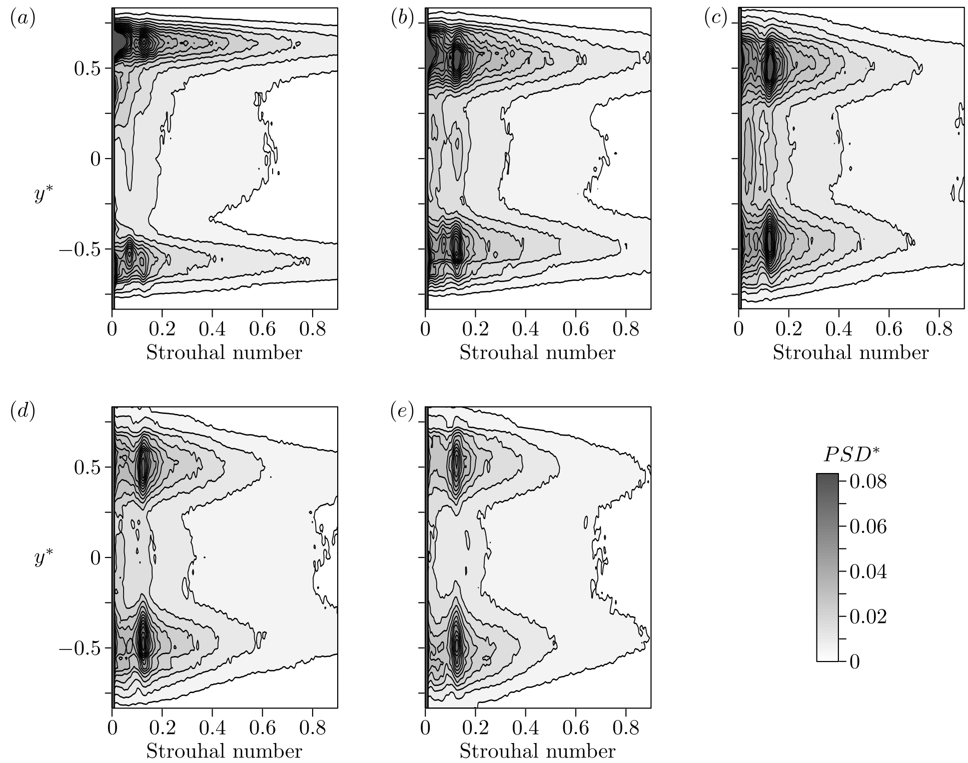

FIGURE 19. Auto-power spectra in the plane $z^* = 0.6$ at $x^* = 1.0$ (*a*), $x^* = 1.5$ (*b*), $x^* = 2.0$ (*c*), $x^* = 2.5$ (*d*), $x^* = 3.0$ (*e*).

The mode is not significant in the mixing layer upstream of the end of the recirculation bubble, *i.e.* for $x^* < 1.5$. Downstream of $x^* = 1.5$, it is more energetic than the large scale structures of turbulence and is particularly clear at $x^* = 2$ and 2.5. The lack of symmetry in figures 19(*a*)–(*b*) is due to the asymmetric intrusion of the hot-wire probe in a region where the flow is likely to be highly sensitive (see figure 1). The probe induces a predominance of the state #P presented in section 3.2.1 and then the energy of the fluctuations of velocity is greater in the $y^* > 0$ region. The symmetry is recovered as soon as the probe is located downstream of $x^* = 2.0$. These results are in agreements with the experiments of Grandemange *et al.* (2012*b*) which indicate that the sensitivity of the wake orientation is concentrated upstream of the end of the recirculation bubble. Similarly, the results plotted in figure 20 show that only the St_2 mode is present in the plane of symmetry $y^* = 0$. These two modes are clearly visible only in the autopower spectra downstream of the end of the recirculation bubble.

To characterize the three-dimensional repartition of these modes, the locations where each frequency is detected are reported in the crossflow planes $x^* = 1.5$, 2.5 and 4: the criterion used to determine whether the St_i mode (with $i \in \{1; 2\}$) is present or not is based on the comparison between the mean energy in the range $\mathrm{St} \in [\mathrm{St}_i - 0.015; \mathrm{St}_i + 0.015]$ and the mean energy in $\mathrm{St} \in [0.040; 0.300]$: the mode is reported when the energy ratio is larger than 1.2. In figures 21, circles (resp. crosses) locate the positions of the hot-wire probe where the mode St_1 (resp.St_2) is detected. The results in the plane $x^* = 1.5$ are displayed in figure 21(*a*); the St_1 mode is mostly found in the lateral mixing layers whereas the St_2 mode is associated with the top and bottom mixing layers; both frequencies are obtained at the frontiers of these regions. It is worth noting a limit on

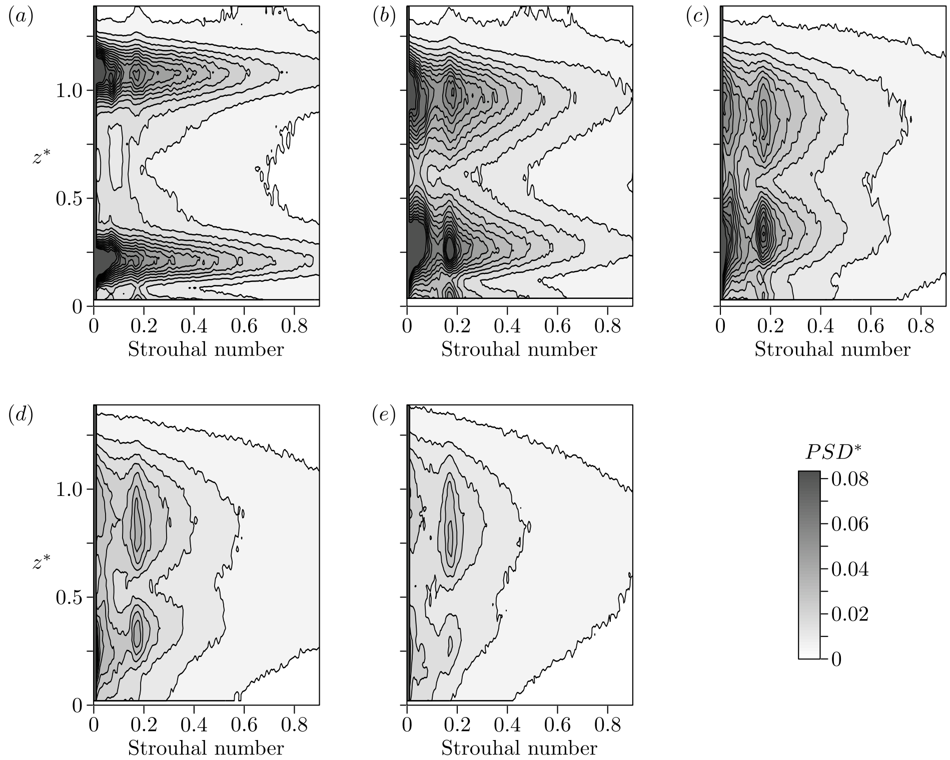

FIGURE 20. Auto-power spectra in the plane $y^* = 0$ at $x^* = 1.0$ (a), $x^* = 1.5$ (b), $x^* = 2.0$ (c), $x^* = 2.5$ (d), $x^* = 3.0$ (e).

the criterion: as the energy of the St_1 mode is in general larger than the St_2 one, the criterion is less selective for the St_1 mode; for example, the St_1 mode may be reported downstream of the lower mixing layer while there is no clear peak visible in figure 20(b). Moving downstream at $x^* = 2.5$ (see figure 21b), the locations are similar, the main difference is the extension of the bottom St_2 region in the y direction. In the plane $x^* = 4$, figure 21(c) indicates that the mode at St_1 remains downstream of the lateral mixing layers whereas the St_2 one separates into three regions: one located downstream of the top mixing layer, the two others are downstream of the bottom corners of the base. As previously seen, there is an adverse pressure gradient on the ground in the plane $y^* = 0$ so that the velocity is reduced in the plane of symmetry. The coherent structures from the bottom trailing edge are then certainly convected with the flow to the sides at $y^* \approx \pm 0.5$.

In order to depict the structure of these modes, cross correlations between two hot-wire probes are performed at the different positions shown in figure 18(b). First, the velocity signals at $A(2.5, 0, 0.9)$ and $A'(2.5, 0, 0.3)$ are studied. The results can be seen in figure 22(a). The coherence is measured close to 0.5 at $\mathrm{St}_2 = 0.174$ with a phase shift of 0.75π. The peak of energy in the autopower spectrum at point A results in coherent structures at St_2 associated with a top / bottom mixing layer interaction. To understand the value of 0.75π, the phase shift at St_2 is studied varying the streamwise position of the second hot-wire position referring to the point A. The result displayed in figure 23 shows that the phase shift linearly depends on the gap in the x direction between the point A and the second probe position. The perfect phase opposition is found at $A''(2.1, 0, 0.3)$. As a consequence, the St_2 mode is an oscillation of the wake in the z direction but the

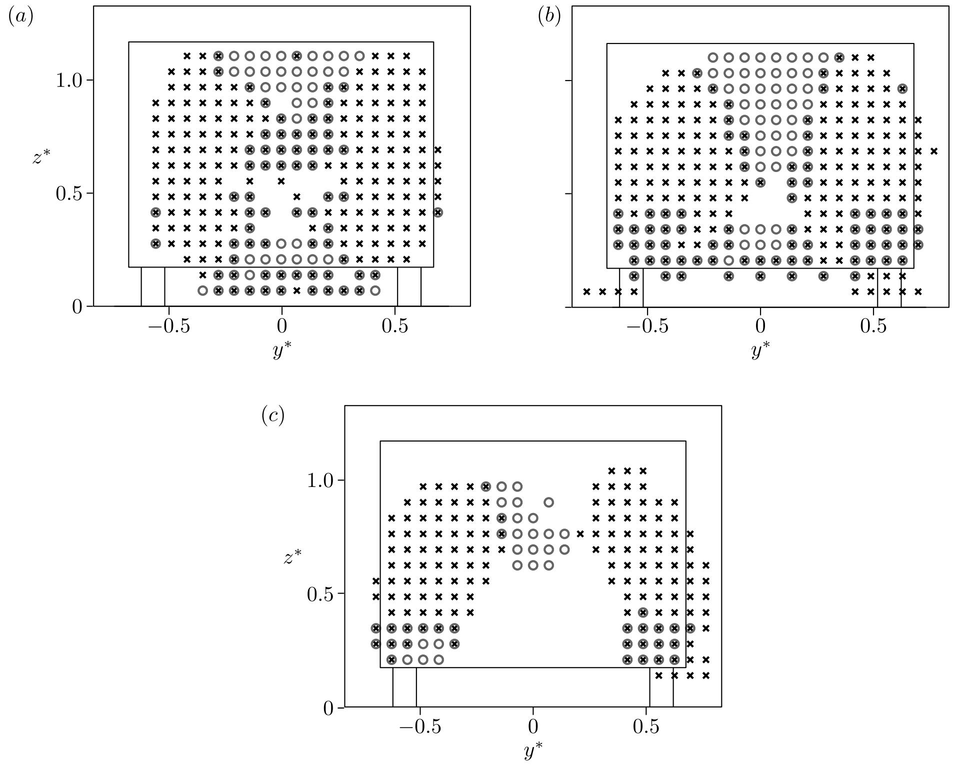

FIGURE 21. Locations where the modes are reported in the planes $x^* = 1.5$ (a), $x^* = 2.5$ (b) and $x^* = 4$ (c): $\mathrm{St}_1 = 0.127$, $\times$; $\mathrm{St}_2 = 0.174$, $\bigcirc$.

presence of the ground affects the phase so that the oscillation is not in an exact phase opposition.

Similar analysis can be made concerning the velocity signals at $B(2.5, 0.5, 0.6)$ and $B'(2.5, -0.5, 0.6)$. The coherence and phase shift defined in (2.4) are plotted in figure 22(b). $r_F(\mathrm{St}_1)$ reaches 0.65 and the corresponding phase is measured at π. The coherent motion associated with the lateral mixing layers is then an oscillation of the wake in the y direction.

Finally, analyzing r_F and ϕ from the velocity measurements at $C(2.5, 0.5, 0.3)$ and $C'(2.5, -0.5, 0.3)$, the signals are found at a coherence of 0.3 for both modes. The signals are in phase opposition at St_1 and in phase at St_2. Thus these values confirm the oscillations of the wake in the y direction at $\mathrm{St}_1 = 0.127$ and in the z direction at $\mathrm{St}_2 = 0.174$.

When these frequencies are normalized respectively by the height of the body and its width, the corresponding Strouhal numbers ($f_1 H/U_0$ and $f_2 W/U_0$) are 0.167 and 0.174. These results must be compared to the analyses of Kiya & Abe (1999) concerning the global modes in the wake of elliptical and rectangular crossflow flat plate. They prove that two modes associated with the interactions of opposite mixing layers coexist. The frequencies roughly rely on the distance between the shear layers at detachment even if no universal Strouhal number can be found. Kiya & Abe (1999) also indicate that the energy is principally measured in the high frequency mode, i.e. the one corresponding to the smaller gap between the shear layers. The main difference with their experiments is the presence of the ground that limits the development of the mode related to the interaction of the top / bottom mixing layers as mentioned in literature (Ruiz *et al.*

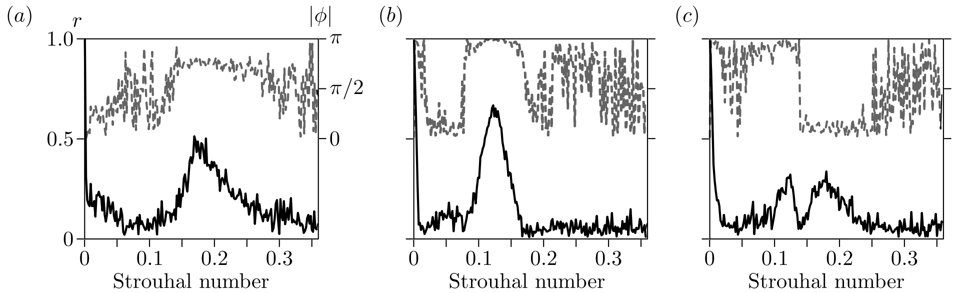

FIGURE 22. Modulus r (continuous line, left scale) and phase ϕ (dashed line, right scale) of the coherence of velocity signals measured at $A(2.5, 0, 0.9)$ and $A'(2.5, 0, 0.3)$ (*a*), $B(2.5, 0.5, 0.6)$ and $B'(2.5, -0.5, 0.6)$ (*b*), $C(2.5, 0.5, 0.3)$ and $C'(2.5, -0.5, 0.3)$ (*c*). For clarity these different positions are displayed in figure 18(*b*).

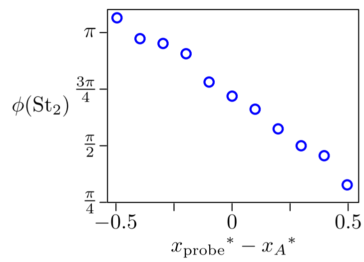

FIGURE 23. (*a*) Phase $\phi(\mathrm{St}_2 = 0.174)$ of the coherence between the velocity signals measured at $A(2.5, 0, 0.9)$ and $(x_{\mathrm{probe}}, 0, 0.3)$.

2009; Khalighi *et al.* 2012). The ground proximity then explains the phase shift between the upper and lower part of the wake at St_2 and also its reduced energy despite the fact that the height of the body is smaller than its width.

4. Discussion

The results presented in section 3 are discussed in the following sections. First, the dynamics of the bi-stability and the ground clearance effect are detailed in section 4.1. The spatial structures of the modes at St_1 and St_2 are considered in section 4.2. Eventually, the effect of the coherent wake motions on drag is discussed in section 4.3.

4.1. *On the bi-stability*

The bi-stability of the wake past this square back geometry is reported here at $\mathrm{Re} = 9.2\ 10^4$ but it has also been observed in various facilities and for an important range of Reynolds numbers: from $\mathrm{Re} = 340$ (Grandemange *et al.* 2012*a*) to $\mathrm{Re} = 2.4\ 10^6$ as presented in Appendix A. The dynamics of this bi-stability are discussed in sections 4.1.1 and 4.1.2; the effect of the ground clearance is detailed in section 4.1.3.

4.1.1. *Random topology shifts*

The long time evolutions is thought to be similar to the one observed by Grandemange *et al.* (2012*b*) in the wake of an axisymmetric geometry or by Herry *et al.* (2011) in the wake of three-dimensional double backward facing steps. In these experiments, the wake has two preferred asymmetric positions; topology shifts occur randomly with very large characteristic time in comparison to the periods of the oscillating global modes.

In the present experiments, the wake shifts between the state #P and #N are analyzed

$\Pr(S_t = \#\mathrm{P}) = 0.514$	$\Pr(S_t = \#\mathrm{N}) = 0.486$
$\Pr(S_t = \#\mathrm{P} \vert S_{t-1} = \#\mathrm{P}) = 0.816$	$\Pr(S_t = \#\mathrm{N} \vert S_{t-1} = \#\mathrm{N}) = 0.806$

TABLE 3. Probabilities of states #P and #N depending on the previous states (precision better than 0.01). $\Pr(\mathrm{E}_1|\mathrm{E}_2)$ is the conditional probability of E_1, given E_2; the events are considered at 1 Hz.

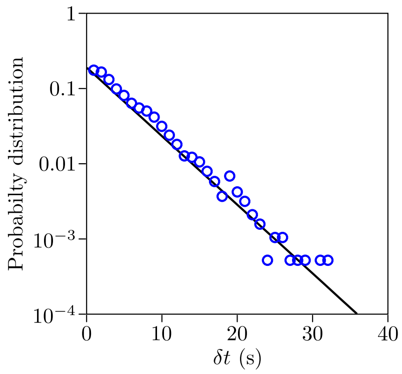

FIGURE 24. Probability distribution of the time between shifts δt. ○, experimental data; —, theoretical law given in (4.3).

from the evaluation of the base pressure gradient in the y direction at 1 Hz overs 10^4 s (see figure 14*a*). The state of the flow at the instant t obtained from the sign of $\partial c_p/\partial y^*$ is denoted $S_t \in \#P, \#N$. The states #P and #N are equiprobable (see table 3), the shifts seem random and appear in average after $T_S = 5.3$ s. Note that $T_S U_0/H \sim 1500$ which implies that the bi-stable dynamic has a time scale three orders of magnitude larger than the typical wake time scale H/U_0. Thus the normalization using U_0 and H seems inappropriate and the following analyses are left in their respective units.

To detail these statistics, the probability distribution of Δt defined as the time between two successive shifts is studied. The distribution follows an exponential law consistent with independent evolutions of the states. Indeed, let $\Pr_{\text{shift}} = \Pr(S_t \neq S_{t-1})$ be the rate of shift per second independent of the instant t. The results presented in table 3 give $\Pr_{\text{shift}} = 0.189$ with

$$\Pr{}_{\text{shift}} = \frac{1}{2}\left[\Pr(S_t = \#\mathrm{P}|S_{t-1} = \#\mathrm{N}) + \Pr(S_t = \#\mathrm{N}|S_{t-1} = \#\mathrm{P})\right]. \qquad (4.1)$$

In case of independent topology shifts, the probability of remaining exactly k seconds in the same state is then given by

$$\Pr(S_{k+1} \neq S_i, \forall i \in \{1..k\}) = \Pr{}_{\text{shift}}\ (1 - \Pr{}_{\text{shift}})^k. \qquad (4.2)$$

As a consequence, the distribution of probability of Δt follows

$$\Pr(\Delta t = \delta t) = 0.189 \times 0.811^{\delta t}. \qquad (4.3)$$

In figure 24, the experimental data are in good agreements with the model given in (4.3). It confirms that the shifts between the topologies #P and #N are random and independent, *i.e.* the succession of states #P and #N behaves like a stationary Markov chain. This point is also consistent with the autopower spectra at B plotted in figure 9(*a*): the repartition of energy for frequencies under 1 Hz follows a power law with an exponent

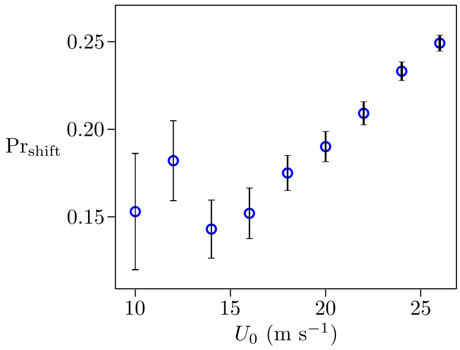

FIGURE 25. Probability to shift $\mathrm{Pr}_{\mathrm{shift}}$ obtained from pressure measurements at 1 Hz as a function of free stream velocity.

close to -2 expected for such random evolutions.
To improve the understanding of this bi-stable behavior, the study of the impact of the free stream velocity on the asymmetry of the states #P and #N and the dynamics of shifts are detailed in section 4.1.2.

4.1.2. *Effect of the free flow velocity*

By changing the flow velocity, the bi-stability has been observed in this facility at Reynolds numbers from 4.6 10^4 to 1.2 10^5. For each Reynolds number, the probability distribution of the base pressure gradient in the y direction presents two preferred positions as seen in figure 14(a). However $\mathrm{Pr}_{\mathrm{shift}}$, which is the rate of shift at 1 Hz, is increasing with the velocity, *i.e.* the mean time between shifts diminishes while the velocity increases (see figure 25). The precision also increases with the velocity since the ratio signal by noise is proportional to ${U_0}^2$ in the measurements of pressure gradients. It remains limited at moderate velocity and the experimental set-up is not appropriate for further quantitative investigation on the dependence of the bi-stability on the free stream velocity.
It is also found that the states #P and #N always correspond to similar values of $\frac{\partial c_p}{\partial y^*} \approx \pm 0.17$. This indicates that the two topologies #P and #N are identical in our range of Reynolds number. Moreover, in section 3.2.1 the signature of the bi-stability is observed only near the afterbody. Therefore, this symmetry breaking behavior seems to be only linked to the shape of the afterbody; this statement is also consistent with the reflectional symmetry breaking of the laminar wake established by Grandemange *et al.* (2012a).
Besides, in these laminar experiments, it is mentioned that no spontaneous topology shift has been observed. The high energy of the large scale turbulent structures may then play a critical role in the probability to shift from one asymmetric state to another. Such an interpretation is in accordance with both the randomness of the shifts and the increasing probability to shift with the Reynolds number.
The observed asymmetric wake is then independent of the Reynolds number but Grandemange *et al.* (2012a) mentioned that it strongly relies on the ground proximity; the effect of the ground clearance on the bi-stability is then investigated in section 4.1.3.

4.1.3. *Effect of the ground clearance*

To clarify the conditions of existence of the bi-stability, experiments are performed at different ground clearances $C^* \in [0; 0.50]$. For each ground clearance, the pressure on the base is recorded every seconds during 3 10^3 s; it enables the measurement of the base

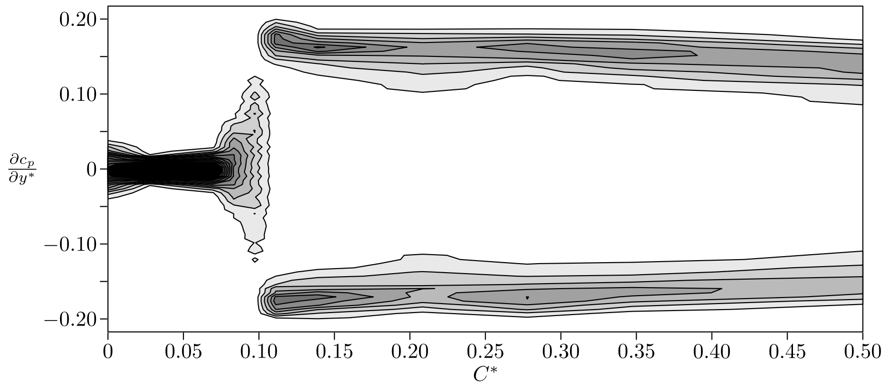

FIGURE 26. Probability density function of the base pressure gradient in the y direction at $y^* = 0$ as a function of the ground clearance C; measurements are performed for $C^* = 0$, 0.03, 0.07, 0.08, 0.10, 0.11, 0.14, 0.21, 0.28, 0.35 and 0.50 with a precision of 0.005, the reference ground clearance is $C^* = 0.17$; contour intervals are 2.

pressure gradients in the y direction at $y^* = 0$ which is a indicator of the wake asymmetry as described in section 3.2.1. For a considered value of C, the probability distribution of $\partial c_p/\partial y^*$ indicates whether the wake has a bi-stable behavior or not: the bi-stability is characterized by two preferred asymmetric positions as in figure 14(a) whereas a stable wake is associated with a probability distribution concentrated around 0. The results shown in figure 26 must be interpreted for a constant value of C^*, the gray levels then correspond to the probability density function (PDF) of $\partial c_p/\partial y^*$ for this value of C^*.

- For $C^* < 0.07$, the PDF is centered on 0 and the most probable event is clearly $\partial c_p/\partial y^* = 0$. The wake is then stable in the symmetric state.
- For $0.07 < C^* < 0.10$, the PDF remains centered on 0 but the peak gradually spreads: for $C^* = 0.10$, the probability density function is almost constant in the range $\partial c_p/\partial y^* \in [-0.10; 0.10]$. Thus, the wake is stable but it progressively loses its preference toward the centered state.
- For $C^* > 0.10$, the PDF presents two clear peaks centered around $\partial c_p/\partial y^* = \pm 0.17$ and this preferred values are independent of the ground clearance at first order. The wake is then bi-stable and the ground clearance has no effect on the preferred degree of asymmetry.

As a result, the bi-stable behavior is strongly linked to the ground clearance: a critical value $C^* = 0.10$ is measured under which the bi-stability is suppressed. It may be associated with a change of topology related to a separation on the ground. Besides, the preference of the flow toward asymmetric states is measured even far from the ground which indicates that the ground effect is not necessary to have preferred asymmetric positions.
Eventually, these results highlight the important impact of the under-body flow on the existence of the bi-stability. In particular, if the support of the geometry limits the under-body flow, it is very likely that the preference of the wake toward asymmetric positions will not be observed.

4.2. *On the structure of the coherent wake motions*

The coherent wake dynamics detailed in section 3.2 are the superposition of three different phenomena:

- the bi-stability in the y direction associated with a random wake offset;
- the lateral shear layer interaction inducing a wake oscillation in the y direction;
- the top / bottom shear layer interaction inducing a wake oscillation in the z direction.

The bi-stable behavior has a long time evolution in front of the oscillating global modes: an asymmetric state (#P or #N) persists in average for hundreds of global mode periods. To be pertinent, the organization of the coherent structures at St_1 and St_2 must then be analyzed for a fixed asymmetric state that has been studied in section 3.2.1 through conditional averaging. In the following, the case of the wake in the state #P is considered; a spatial organization of the coherent oscillations of the wake is proposed from the asymmetric conditional statistics of the flow but also considering the visualizations of the laminar wake in Grandemange *et al.* (2012*a*).

The oscillating global mode in the z direction is in phase opposition at the end of the recirculation region but phase shift gradually evolves. Indeed, $\phi(\mathrm{St}_2)$ measured between two signals of velocity in the plane $y^* = 0$ downstream of the top and bottom mixing layers is progressively measured at 0.95π, 0.75π and 0.65π for $x^* = 2.0$, 2.5 and 3.0 respectively. This phase shift evolution is associated with the difference in the convecting velocity between the upper and lower parts of the wake because of the ground presence. This point is clearly visible in the laminar experiments of Grandemange *et al.* (2012*a*) (see figure 2b) when the wake is in the transient unsteady symmetric regime. A structure of alternative vortex loops from the upper and lower part of the recirculation region is probable but there is no reason for them to have similar intensities.
Besides, the confrontation of the Reynolds shear stresses from global and local statistics in the top and bottom mixing layer (figures 8*c* and 13*c*) tends to indicate that the unsteady global mode is only slightly affected by the bi-stability: at first sight, its structure is independent of the asymmetric state #P or #N. A sketch interpreting the spatial structure of this mode is then displayed in figure 27(*a*).

On the other hand, the wake oscillation in the y direction remains in phase opposition in the wake but it is strongly affected by the selection of the asymmetric state. The figures 13(*a*)–(*b*) show that the fluctuations of velocity are concentrated on one side of the recirculation region. A structure of parallel loops is then expected, oriented toward the $y^* > 0$ regions (resp. $y^* < 0$) when the wake is fixed in the asymmetric state #P (resp. #N). However this point could not be clearly evidenced because of the high difficulty to separate these structures from the z oscillations in the spatial domain. A sketch of this mode is presented in figure 27(*b*).

The organization of the wake is then the combination of these two oscillating global modes. It is impossible to present a global sketch as the associated frequencies are different. A certain continuity between the vortices shed from the top / bottom and side faces is presumed but such a dynamics would necessarily be associated with vortex dislocations. Moreover, these coherent dynamics are masked by the turbulence as the energy associated with these modes is small. In the autopower spectra at A and B presented in figure 18(*a*), the increase of energy associated with the peaks at St_1 and St_2 are measured respectively at 7% and 3% of the total energy. For comparison, in the turbulent wake past a circular cylinder at similar Reynolds numbers, the contributions of the coherent and incoherent velocity fluctuations to the Reynolds stresses are equivalent (Cantwell & Coles 1983; Balachandar *et al.* 1997).

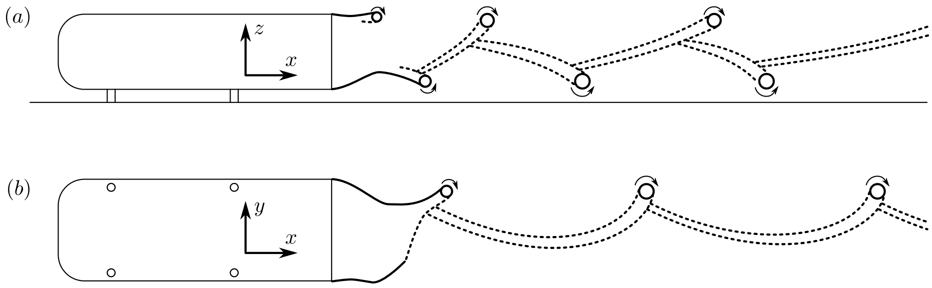

FIGURE 27. Sketch of the structure of the oscillating global modes in the z direction (a) and in the y direction (b) while the wake is fixed in the state #P.

Finally, these results can be confronted to the descriptions of the wake reported in literature. First, the vertical wake oscillation is likely to be the one reported by Khalighi *et al.* (2012) at St = 0.17 downstream of the recirculation region with a peak of energy particularly clear when the probe is in the plane of symmetry. Second, the peaks of energy in the lateral and vertical forces observed in the numerical simulations of Bayraktar *et al.* (2001) might be associated with similar dynamics even if the Strouhal numbers do not correspond to the present results. On the contrary, the low frequency pumping mode was not observed here and these results prove that the interpretation of interactions between the upper and the lower part of the toric recirculation structure is not relevant: a toric topology of the wake is not consistent with the time-scale of a coherent motion at St $\sim$ 0.07.

4.3. *On the drag sources*

From these experiments, some issues on the drag sources can be addressed: the contributions of the oscillating modes and of the bi-stability are considered in sections 4.3.1 and 4.3.2 respectively.

4.3.1. *Impact of the oscillating global modes*

In literature, the presence of global modes in wakes often impacts the drag significantly. In the von-Kármán wakes past cylinders, 35% to 55% of the Reynolds stresses are related to the vortex shedding activity (Cantwell & Coles 1983). Over such bi-dimensional geometries, the mechanisms responsible for the closure of the recirculation region are critical issues as the length of the mean recirculation bubble is directly linked to the base pressure (Roshko 1993; Parezanović & Cadot 2012). Exploring the effects of a small control cylinder in the wake of a "D"-shaped bi-dimensional geometry, Cadot *et al.* (2009) and Parezanović & Cadot (2012) showed that for the undisturbed case, the maximum amplitude of the mode is located in the mixing layers before the end of the recirculation region whereas for optimal disturbed cases the energy of the mode is reduced and reported downstream of the recirculation region. Thus, when efficiently disturbed, the mode is less responsible for the closure of the recirculation region which leads to an increased recirculation length and drag reductions.
The results presented in section 3.2.2 highlight coherent oscillations of the wake in both the y and the z directions. However, the autopower spectra show that the energy associated with these modes is small in comparison with the turbulent activity of the mixing layers, especially around the separatrix of the recirculation bubble (see figures 19a and 20a). Therefore, the contribution of these oscillating modes to the recirculation physics is limited and not sufficient to affect the drag significantly.

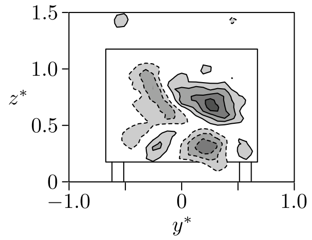

FIGURE 28. Contours of streamwise vorticity in the plane $x^* = 2$ for the state #P. Continuous and dashed lines are respectively positive and negative values, contour intervals are 0.5, contour 0 is not plotted.

These observations tend to turn drag reduction strategies toward the control of the growth rate of the turbulent mixing layers in the close wake (Greenblatt & Wygnanski 2000) rather than the control of the global mode activity.

4.3.2. *Impact of the bi-stability*

Because of the bi-stability, the instantaneous wake is off the reflectional plane of symmetry. An aerodynamic force is present in the y direction while the flow is in the state #P or #N but counterbalance in average due to the equipresence of the two states. Nevertheless, the mean drag corresponds to the drag of the asymmetric states which is enhanced by this side force. Indeed, part of the drag is induced by the forces F_y and F_z and is linked to the pair of vortices visible in the streamwise vorticity map presented in figure 28. These phenomena of induced drag are well known in aeronautics but also in the car industry. For example, the Ahmed geometry (Ahmed *et al.* 1984) with a 25° slant angle is a high drag / high lift configuration that is also characterized by a pair of intense counter-rotating vortices in the wake (Beaudoin *et al.* 2004). For comparison, the normalized circulation of one vortex is estimated around ± 0.2 in the present asymmetric case in the plane $x^* = 2.0$ and at ± 0.8 in the plane $x^* = 1.7$ in the 25° case from the data of Lienhart & Becker (2003): the intensity of the pair of vortices is then much smaller but remains significant. However, in the present case, the contribution of the asymmetry in the y direction to the drag is difficult to estimate with a reasonable precision.

The influence of crossflow forces F_y and F_z can be seen for the asymmetric states in figure 11(c) but the streamlines in the average symmetric flow exclusively marks the lift influence (see figure 2d). The effect of the unsteady side force is measured in the mean symmetric flow through the Reynolds stresses since part of the fluctuations of velocity is related to the differences in the mean velocities of the states #P and #N. This point is particularly clear comparing the global and conditional statistics in figures 7(b) and 12(b): the maximum of $\langle {u'_y}^{*2} \rangle$ is measured respectively inside and outside the recirculation region in the plane $z^* = 0.6$. As a result, it can be stated that the mean force but also its fluctuations must be considered to analyze the induced drag of three-dimensional geometries.

5. Concluding remarks

The flow around the square-back Ahmed geometry is characterized at Reynolds number 9.2 10^4. First, a boundary layer detachment occurs on the four faces of the forebody due to a high adverse pressure gradient; then, a massive recirculation responsible for a dominant part of the drag is reported on the base. The equilibrium of the wake in the

z direction is affected by the presence of the ground but the low pressure region in the wake, located around the time-averaged recirculation structures, preserves a toric shape. However, it is crucial to be clear in the interpretation of the toric organization of the recirculation region: it is a long time-averaged vision and it does not reflect the topology of the flow because the wake has a bi-stable behavior. The recirculation region has two preferred reflectional symmetry breaking positions that leads to the statistical symmetric wake. The succession of these asymmetric states is random and behaves like a stationary Markov chain. This leads to an unsteady side forcing which must be responsible for part of the drag. Moreover, this bi-stability is independent of the Reynolds number in turbulent regimes and the reflectional symmetry breaking is reported as a bifurcation of the laminar wake at $\mathrm{Re} = 340$ (Grandemange *et al.* 2012*a*).
In addition, the interactions of the opposed shear layers induce oscillations of the wake at Strouhal numbers close to 0.17 when normalized by their respective gap. The presented results tend to indicate that the modes are convected with the mean flow. However, these modes are not particularly energetic and only represent a negligible part of the Reynolds stresses around the recirculation region. Their impact on the base pressure is certainly reduced which should be considered for future control strategies.

The bi-stable behavior may be an important characteristic of turbulent wakes. It has been observed in the wake past different three-dimensional geometries but the circumstances of existence still need to be clarified. Besides, these results show the risks of adjusting the experimental instrumentation of a geometry on its symmetries. On the other hand, in the framework of numerical simulations, a limited physical time of calculation may prevent the flow from reaching the asymmetric states and then lead to unstable or transient wake solutions.
Another consequence of this bi-stability is that a perfect symmetry of the measurements is very difficult to obtain, especially with limited measurement durations. Indeed, the equipresence of the asymmetric states #P and #N is highly dependent on the quality of the reflectional symmetry of the set-up. Further work on this geometry is performed to analyze the sensitivity of the flow to local disturbance. Besides, these experiments will provide quantitative information on the contribution of the asymmetry to the drag. The results are to be presented in a second communication.

$C_x = 0.308$	$Std(c_x) = 0.004$
$C_y = 0.004$	$Std(c_y) = 0.015$
$C_z = -0.056$	$Std(c_z) = 0.006$

TABLE 4. Mean and standard deviation of the aerodynamic forces on the large scale model.

Appendix A. Large scale experiments

Experiments are performed in the full scale aeroacoustic wind-tunnel of GIE S2A at Montigny-Le-Bretonneux (Waudby-Smith *et al.* 2004). The test section is a 3/4 open jet with a cross section of 24 m^2. Four wheel spinners and a central rotating belt enable to operate under rolling road conditions.
Like in the previous study, the geometry corresponds to the square-back Ahmed body but at scale 4, *i.e.* sixteen times larger than the model presented in figure 1, to matches the dimensions of a real vehicle. The main difference is that for practical reasons, the cylindrical supports have been replaced by four wheels. The ground clearance is set at 190 mm. The inlet and the moving belt velocities are set at 33.3 m s^{-1}. The Reynolds number is then 2.5 10^6. The forces are measured through the six-component balance. Besides, pressure sensors are placed on the geometry and a flying hot-wire probe is used to catch the dynamics of the wake.

The force measurements are presented in table 4. The drag is measured at 0.302 which is larger than the previous result and than the one presented in Ahmed *et al.* (1984) but remains close to the values given in literature. As measured in the small scale experiments, the lift is small but negative and the force in the y direction is close to 0. Nevertheless, a first indicator of a bi-stable behavior can be seen in the values of the force fluctuations: the fluctuations of the force in the y direction are much larger than in the x and z directions.
The bi-stability of the flow is confirmed by the pressure measurements presented in figure 29; the pressure on the forebody is constant whereas the pressure on the base presents unsteadiness. The pressure coefficient at the taps #3 and #4 is measured mostly either around -0.19 or around -0.27 and they evolve in phase opposition. This leads to a permanent pressure gradient in the y direction estimated at ± 0.18 which is very close to the measurement presented in section 3.2.1. Changes in the sign of this gradient correspond to long time evolutions (typically 20 s) and their dynamics seem random as described in section 4.1.1.

Eventually, it is worth noticing the two following points. First, the unsteady global modes presented in section 3.2.2 are highly difficult to catch with a flying hot-wire probe. The contribution of the modes based on shear layer interaction to the fluctuations of velocities may be reduced due to the increase of the Reynolds number. Second, even at this high Reynolds number, viscous paint visualizations show that boundary layer separations occur at the end of the rounding of the forebody at least on the top and lateral face but their expansion in the streamwise direction is small: less than 50 mm, *i.e.* $0.01L$.

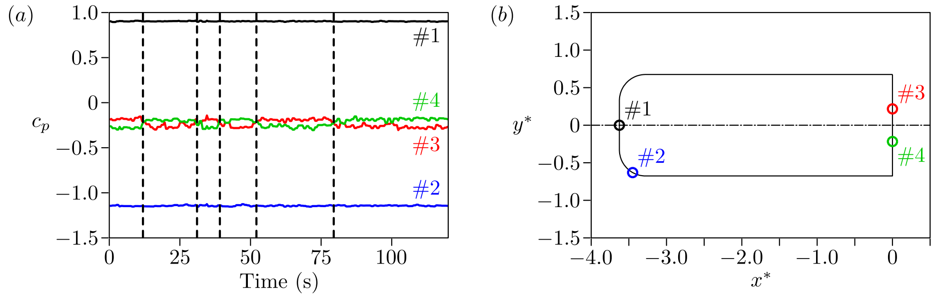

FIGURE 29. Time evolution of the pressure on the large scale Ahmed geometry (a) and positions of the corresponding pressure taps (b) in the plane $z^* = 0.67$; dashed lines mark the topology shifts.

Acknowledgements

The authors are grateful to the CNRT R2A for supporting the large sale experiments at GIE S2A; this partnership between industrial and academic actors addresses aerodynamic and aeroacoustic issues of land vehicles.

REFERENCES

AHMED, SR, RAMM, G. & FAITIN, G. 1984 Some salient features of the time-averaged ground vehicle wake. *Tech. Rep.*. Society of Automotive Engineers, Inc., Warrendale, PA.

BALACHANDAR, S., MITTAL, R. & NAJJAR, FM 1997 Properties of the mean recirculation region in the wakes of two-dimensional bluff bodies. *Journal of Fluid Mechanics* **351**, 167–199.

BAYRAKTAR, I., LANDMAN, D. & BAYSAL, O. 2001 Experimental and computational investigation of ahmed body for ground vehicle aerodynamics .

BEAUDOIN, J.F. & AIDER, J.L. 2008 Drag and lift reduction of a 3D bluff body using flaps. *Experiments in Fluids* **44** (4), 491–501.

BEAUDOIN, JF, CADOT, O., AIDER, JL, GOSSE, K., PARANTHOËN, P., HAMELIN, B., TISSIER, M., ALLANO, D., MUTABAZI, I., GONZALES, M. *et al.* 2004 Cavitation as a complementary tool for automotive aerodynamics. *Experiments in fluids* **37** (5), 763–768.

BERGER, E., SCHOLZ, D. & SCHUMM, M. 1990 Coherent vortex structures in the wake of a sphere and a circular disk at rest and under forced vibrations. *Journal of Fluids and Structures* **4** (3), 231–257.

BRUNEAU, C.H., CREUSE, E., DEPEYRAS, D. & GILLIERON, P. 2011 Active procedures to control the flow past the ahmed body with a 25 rear window. *International Journal of Aerodynamics* **1** (3), 299–317.

BRUNEAU, C.H., CREUSÉ, E., DEPEYRAS, D., GILLIÉRON, P. & MORTAZAVI, I. 2010 Coupling active and passive techniques to control the flow past the square back ahmed body. *Computers & Fluids* **39** (10), 1875–1892.

CADOT, O., THIRIA, B. & BEAUDOIN, J. F. 2009 Passive drag control of a turbulent wake by local disturbances. *IUTAM Bookseries*, vol. 14, pp. 529–537. IUTAM Symposium on Unsteady Separated Flows and their Control, Corfu, GREECE, JUN 18-22, 2007.

CANTWELL, B. & COLES, D. 1983 An experimental study of entrainment and transport in the turbulent near wake of a circular cylinder. *Journal of Fluid Mechanics* **136**, 321–374.

DUELL, E.G. & GEORGE, AR 1993 Measurements in the unsteady near wakes of ground vehicle bodies. *Tech. Rep.*. Society of Automotive Engineers, 400 Commonwealth Dr, Warrendale, PA, 15096, USA,.

DUELL, E.G. & GEORGE, AR 1999 Experimental study of a ground vehicle body unsteady near wake. *SAE transactions* **108** (6; PART 1), 1589–1602.

FOURRIÉ, G., KEIRSBULCK, L., LABRAGA, L. & GILLIÉRON, P. 2011 Bluff-body drag reduction using a deflector. *Experiments in Fluids* **50** (2), 385–395.

FRANCK, G., NIGRO, N., STORTI, M. & DELIA, J. 2009 Numerical simulation of the Ahmed vehicle model near-wake. *Latin American Applied Research* **39** (4).

Gilliéron, P. & Kourta, A. 2010 Aerodynamic drag reduction by vertical splitter plates. *Experiments in fluids* **48** (1), 1–16.

Grandemange, M., Cadot, O. & Gohlke, M. 2012*a* Reflectional symmetry breaking of the separated flow over three-dimensional bluff bodies. *Phys. Rev. E* **86**, 035302.

Grandemange, M, Parezanović, V, Gohlke, M & Cadot, O 2012*b* On experimental sensitivity analysis of the turbulent wake from an axisymmetric blunt trailing edge. *Physics of fluids* **24**, 035106.

Greenblatt, D. & Wygnanski, I.J. 2000 The control of flow separation by periodic excitation. *Progress in Aerospace Sciences* **36** (7), 487–545.

Herry, B.B., Keirsbulck, L & Paquet, J.B. 2011 Flow bistability downstream of three-dimensional double backward facing steps at zero-degree slideslip. *ASME Transactions Journal of Fluids Engineering* **133** (054501), 1–4.

Hucho, WH 1998 *Aerodynamics of Road Vehicles*. SAE.

Khalighi, B., Chen, K.H. & Laccarino, G. 2012 Unsteady aerodynamic flow investigation around a simplified square-back road vehicle with drag reduction devices. *Journal of fluids engineering* **134** (6).

Khalighi, B., Zhang, S., Koromilas, C., Balkanyi, SR, Bernal, L.P., Iaccarino, G. & Moin, P. 2001 Experimental and computational study of unsteady wake flow behind a bluff body with a drag reduction device. *SAE paper* .

Kiya, M. & Abe, Y. 1999 Turbulent elliptic wakes. *Journal of Fluids and Structures* **13** (7-8), 1041–1067.

Krajnović, S. & Davidson, L. 2005 Flow around a simplified car, part 2: understanding the flow. *Journal of Fluids Engineering* **127**, 919.

Lawson, N. J., Garry, K. P. & Faucompret, N. 2007 An investigation of the flow characteristics in the bootdeck region of a scale model notchback saloon vehicle. *Proceedings of the institution of mechanical engineers PART D-journal of automobile engineering* **221** (D6), 739–754.

Lienhart, H. & Becker, S. 2003 Flow and turbulence structure in the wake of a simplified car model. *SAE transactions* **112** (6), 785–796.

Littlewood, R. & Passmore, M. 2010 The Optimization of Roof Trailing Edge Geometry of a Simple Square-Back. *SAE paper* .

Pao, H.P. & Kao, T.W. 1977 Vortex structure in the wake of a sphere. *Physics of Fluids* **20**, 187.

Parezanović, V. & Cadot, O. 2012 Experimental sensitivity analysis of the global properties of a 2D turbulent wake. *Journal of Fluid Mechanics* **693**, 115–149.

Pujals, G., Depardon, S. & Cossu, C. 2010 Drag reduction of a 3d bluff body using coherent streamwise streaks. *Experiments in fluids* **49** (5), 1085–1094.

Roshko, A. 1993 Perspectives on bluff body aerodynamics. *Journal of Wind Engineering and Industrial Aerodynamics* **49** (1-3), 79–100.

Rouméas, M., Gilliéron, P. & Kourta, A. 2009 Analysis and control of the near-wake flow over a square-back geometry. *Computers & Fluids* **38** (1), 60–70.

Ruiz, T., Sicot, C., Brizzi, L.E., Laumonier, J., Borée, J. & Gervais, Y. 2009 Unsteady near wake of a flat disk normal to a wall. *Experiments in fluids* **47** (4), 637–653.

Sakamoto, H. & Haniu, H. 1990 A study on vortex shedding from spheres in a uniform flow. *ASME, Transactions, Journal of Fluids Engineering* **112**, 386–392.

Spohn, A. & Gilliéron, P. 2002 Flow separations generated by a simplified geometry of an automotive vehicle. In *Congress IUTAM Symposium on Unsteady Separated Flows*.

Taneda, S. 1978 Visual observations of the flow past a sphere at Reynolds numbers between 104 and 106. *Journal of Fluid Mechanics* **85** (01), 187–192.

Wassen, E., Eichinger, S. & Thiele, F. 2010 Simulation of active drag reduction for a square-back vehicle. *Active Flow Control II* pp. 241–255.

Waudby-Smith, P., Bender, T. & Vigneron, R. 2004 The gie s2a full-scale aero-acoustic wind tunnel. *SAE transactions* **113** (6), 449–461.

Yun, G., Kim, D. & Choi, H. 2006 Vortical structures behind a sphere at subcritical Reynolds numbers. *Physics of Fluids* **18**, 015102.